AMERICAN SOCIETY FOR MICROBIOLOGY | mSystems®

RESEARCH ARTICLE

Integrative Genome-Scale Metabolic Modeling Reveals Versatile Metabolic Strategies for Methane Utilization in *Methylomicrobium album* BG8

Juan C. Villada,[a] Maria F. Duran,[a] Chee Kent Lim,[a] Lisa Y. Stein,[b] Patrick K. H. Lee[a,c]

[a]School of Energy and Environment, City University of Hong Kong, Hong Kong SAR, China
[b]Department of Biological Sciences, University of Alberta, Edmonton, Alberta, Canada
[c]State Key Laboratory of Marine Pollution, City University of Hong Kong, Hong Kong SAR, China

ABSTRACT *Methylomicrobium album* BG8 is an aerobic methanotrophic bacterium with promising features as a microbial cell factory for the conversion of methane to value-added chemicals. However, the lack of a genome-scale metabolic model (GEM) of *M. album* BG8 has hindered the development of systems biology and metabolic engineering of this methanotroph. To fill this gap, a high-quality GEM was constructed to facilitate a system-level understanding of the biochemistry of *M. album* BG8. Flux balance analysis, constrained with time-series data derived from experiments with various levels of methane, oxygen, and biomass, was used to investigate the metabolic states that promote the production of biomass and the excretion of carbon dioxide, formate, and acetate. The experimental and modeling results indicated that *M. album* BG8 requires a ratio of ~1.5:1 between the oxygen- and methane-specific uptake rates for optimal growth. Integrative modeling revealed that at ratios of >2:1 oxygen-to-methane uptake flux, carbon dioxide and formate were the preferred excreted compounds, while at ratios of <1.5:1 acetate accounted for a larger fraction of the total excreted flux. Our results showed a coupling between biomass production and the excretion of carbon dioxide that was linked to the ratio between the oxygen- and methane-specific uptake rates. In contrast, acetate excretion was experimentally detected during exponential growth only when the initial biomass concentration was increased. A relatively lower growth rate was also observed when acetate was produced in the exponential phase, suggesting a trade-off between biomass and acetate production.

IMPORTANCE A genome-scale metabolic model (GEM) is an integrative platform that enables the incorporation of a wide range of experimental data. It is used to reveal system-level metabolism and, thus, clarify the link between the genotype and phenotype. The lack of a GEM for *Methylomicrobium album* BG8, an aerobic methane-oxidizing bacterium, has hindered its use in environmental and industrial biotechnology applications. The diverse metabolic states indicated by the GEM developed in this study demonstrate the versatility in the methane metabolic processes used by this strain. The integrative GEM presented here will aid the implementation of the design-build-test-learn paradigm in the metabolic engineering of *M. album* BG8. This advance will facilitate the development of a robust methane bioconversion platform and help to mitigate methane emissions from environmental systems.

KEYWORDS methanotroph, methane oxidation, systems biology, integrative modeling, flux balance analysis, fermentation, biotechnology

Anthropogenic activities have led to significant increases in atmospheric methane (1), which contributes to climate change and perturbs the global carbon cycle (2). Nevertheless, methane derived from renewable sources is an attractive substrate in the

Editor Karoline Faust, KU Leuven

Address correspondence to Patrick K. H. Lee, patrick.kh.lee@cityu.edu.hk.

The authors declare no conflict of interest.

Received 22 January 2022
Accepted 21 February 2022
Published 8 March 2022

production of value-added products (3–5), and methane conversion processes represent a promising trend in bioindustry (6, 7). Methanotrophic bacteria utilize methane as their source of carbon and energy, and these microorganisms have become increasingly important in the biomanufacturing of valuable chemical compounds (4, 8–10). Although methanotrophic species are metabolically active under both aerobic and anaerobic conditions (11–14), considerations of cost, sustainability, and environmental impact have led to a preference for aerobic methane-oxidizing bacteria in large-scale biorefining applications (15, 16).

Methylomicrobium album BG8 (formerly known as *Methylobacter albus*, *Methylomonas albus*, or *Methylomonas alba*) is an obligate aerobic, Gram-negative, gammaproteobacterial methanotroph that uses methane or methanol as its sole source of carbon and energy (17). A DNA-DNA hybridization study revealed high levels of similarity between its genome and those of *Methylomicrobium agile* ATCC 35068 (99.16%), *Methylotuvimicrobium alcaliphilum* 20Z (75.69%), and *Methylotuvimicrobium buryatense* 5G (76.64%) (18). Recent phylogenomic analyses based on the average amino acid identity and average nucleotide identity have shown that *M. album* BG8 is also closely related to *Methylomicrobium* (formerly *Methylosarcina*) *lacus* LW14 (19). *M. album* BG8 has been isolated from swampy soils and freshwater sediments (18, 20) and has been widely studied due to its importance in environmental microbiology for bioremediation of different environmental pollutants (21–23). Through recent physiological and omics analyses, *M. album* BG8 has also been identified as a promising microbial cell factory (24, 25) for applications in the methane-based biotechnology industry (26).

The current metabolic characterization of methanotrophic bacteria suggests there are three main groups (27). Methanotrophs in group I (*Gammaproteobacteria*) utilize the ribulose monophosphate (RuMP) cycle to metabolize formaldehyde derived from methane oxidation, group II (*Alphaproteobacteria*) members direct the carbon flux resulting from the oxidation of methane to formate to a complete serine cycle, and group III (*Verrucomicrobia*) members possess a complete Calvin-Benson-Bassham cycle for carbon dioxide utilization. The metabolic engineering of methanotrophs has enabled advances in the biotechnology of methane conversion to produce succinate (28), 3-hydroxypropionic acid (29), 2,3-butanediol (30), putrescine (9), α-humulene (31), cadaverine (32), lysine (32), shinorine (33), and acetoin (33). These laboratory achievements have been aided by the results of genome-scale metabolic model (GEM)-based simulations, which are used to enhance the system-level understanding of methanotrophy. Thus far, GEMs of nine methanotrophic species have been constructed, including three group I species [*Methylotuvimicrobium buryatense* 5G(B1) (34), *Methylotuvimicrobium alcaliphilum* 20Z (35), and *Methylococcus capsulatus* Bath (36, 37)] and six group II species (*Methylocystis hirsuta* [38], *Methylocystis* sp. strain SC2 [38], *Methylocystis* sp. strain SB2 [38], *Methylocystis parvus* OBBP [39], *Methylocella silvestris* [40], and *Methylosinus trichosporium* OB3b [41]). Although some of these GEMs have been validated using growth yields, methane- and oxygen-specific uptake rates (38), transcriptomics data (34), or enzyme kinetics (35), most do not contain other integrated experimental data.

Despite the potential of *M. album* BG8 as a tool in environmental and industrial biotechnology, no GEM of this methanotroph has been developed; therefore, an integrative system-level understanding of methanotrophy in this strain remains lacking. In this study, a high-quality GEM of *M. album* BG8 was constructed by stringently following well-established systems biology protocols (42, 43). Furthermore, an integrative modeling framework was applied, wherein experimental time-series growth and compound uptake and excretion data collected under different initial methane and oxygen headspace percentages and biomass concentrations were integrated with the initial GEM to construct parametrized GEMs. Subsequently, the metabolic states that promote biomass production and carbon dioxide, formate, and acetate excretion were identified through a flux balance analysis (FBA). The study findings provide novel insight into the metabolic versatility

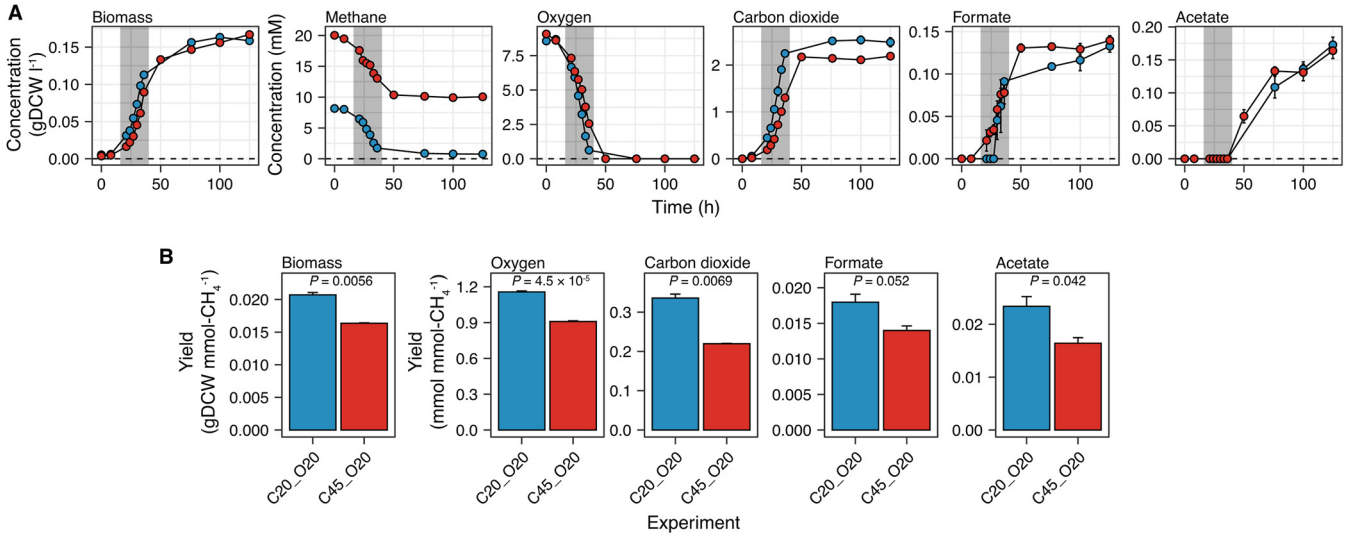

FIG 1 Effects of different initial methane headspace percentages on *Methylomicrobium album* BG8 in culture. (A) Time-series concentration profiles of biomass production, compound consumption, and compound excretion. The gray-shaded region indicates the estimated exponential phase (~16 h to 40 h). (B) Biomass yields, oxygen uptake, and metabolite excretion throughout the culture period. *P* values were determined using the two-sided *t* test. In all panels, the data are shown as the mean values from biological triplicates, and the error bars represent the standard errors. The initial conditions with 20% methane and 20% oxygen (C20_O20) or 45% methane and 20% oxygen (C45_O20) are indicated in blue and red, respectively. In all panels, the same labeling notation is used to denote the experimental conditions, with C representing methane, O representing oxygen, and the following number indicating the initial percentage (vol/vol) in the headspace.

of *M. album* BG8 and highlight the associations between biomass production and organic compound excretion.

RESULTS

Conversion between the OD and DCW. A linear regression model was established between gram of dry cell weight (gDCW) liter^{-1} and optical density at 600 nm (OD_{600}) to calculate the DCW from a measured OD_{600} value. The model with a *y* intercept at the origin produced the best fit (see Fig. S1 in the supplemental material), yielding the equation gDCW liter^{-1} = 0.26 × OD_{600}.

Excess methane did not favor metabolite production. Aerobic methane oxidation, which is catalyzed by the particulate methane monooxygenase in *M. album* BG8, requires an equimolar ratio of oxygen to methane. We first hypothesized that excess methane in a batch culture of *M. album* BG8 favors growth. To test this hypothesis, we characterized the effects of two initial methane (20% [0.41 mmol] or 45% [1.0 mmol]) and oxygen (20% [0.43 mmol]) headspace ratios on metabolite excretion and biomass production. The time-series profiles in Fig. 1A demonstrate that a notable amount of methane remained in the culture with 45% initial methane, and that the final concentrations of biomass and excreted products were not significantly different between the cultures grown under different headspace ratios (*t* test, 5% threshold for *P* value) (Fig. 1A). Contrary to our hypothesis, excess methane significantly reduced (*t* test, $P < 0.05$) not only the biomass yield but also the oxygen uptake and carbon dioxide and acetate excretion yields (Fig. 1B). Although the formate yield was also reduced, this difference was not statistically significant.

Oxygen availability strongly influenced biomass production and organic compound excretion. After determining that excess methane did not favor metabolite excretion, we tested the effects of oxygen availability (range, 5% to 25%) on the metabolism and growth of *M. album* BG8 under 20% methane. The time-series profile in Fig. 2A shows that the initial oxygen headspace percentage significantly affected the dynamics of biomass production and organic compound excretion. The highest concentration of oxygen led to an increased consumption of methane and the highest concentration of excreted organic compounds in culture (Fig. 2A). Interestingly, acetate was only detected after approximately 50 h in cultures subjected to all conditions except 5% oxygen (~36

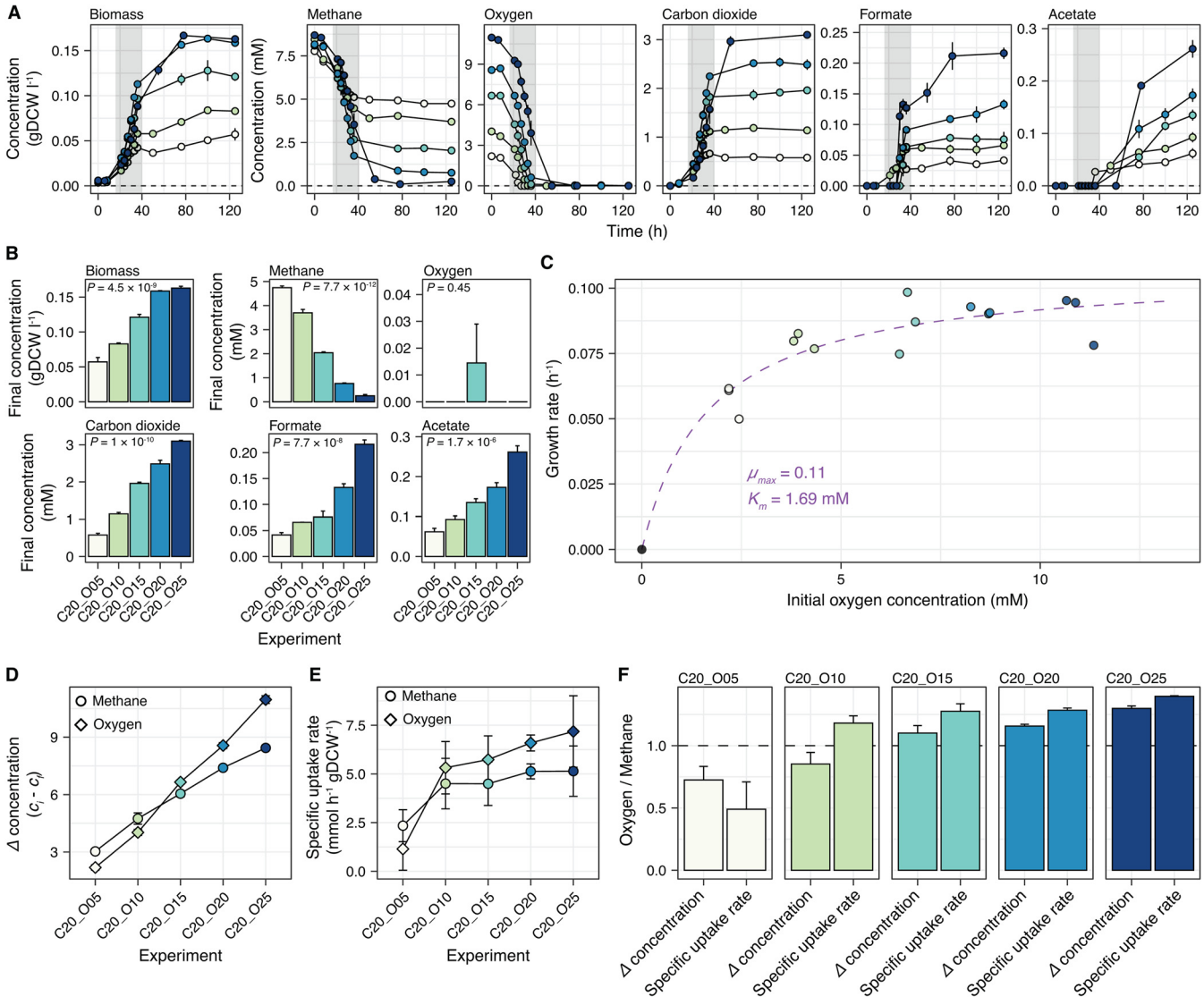

FIG 2 Effects of different initial oxygen headspace percentages on *Methylomicrobium album* BG8 in culture. (A) Time-series concentration profiles of biomass production, compound consumption, and compound excretion. The gray-shaded region indicates the estimated exponential phase (~16 h to 40 h). (B) The concentrations of biomass, consumed compounds, and excreted compounds at the final time point. (C) Growth kinetics with respect to the initial oxygen concentration. The fitted line represents the Monod kinetic model. (D) Changes in methane and oxygen concentrations throughout the culture period. (E) Specific methane and oxygen uptake rates in each culture. Error bars represent the upper and lower bounds of the estimate (99% confidence interval). (F) Comparison of the ratio between the changes in the concentrations of oxygen and methane with the ratio of oxygen-to-methane specific uptake rates. For panels A, B, and D, the data are shown as the mean values from biological triplicates, and the error bars represent the standard errors. In all panels, the color gradient represents the different initial percentages of oxygen (5% to 25%) in 5% increments with 20% methane.

h; Fig. 2A). The final biomass, carbon dioxide, formate, and acetate concentrations were significantly affected by the initial oxygen headspace percentage (analysis of variance [ANOVA], $P < 0.05$; Fig. 2B). In terms of yields, all were significantly affected (ANOVA, $P < 0.05$) except biomass concentration (Fig. S2). Oxygen was practically depleted from all of the cultures at the end of the experiment (120 h; Fig. 2B).

The growth kinetics of the cultures, assuming oxygen was the only limiting substrate, were determined by fitting a Monod kinetic model, resulting in a maximum growth rate (μ_{max}) of 0.11 h^{-1} (95% confidence interval [CI_{95}] = 0.09 to 0.12) and a half-saturation constant (K_m) of 1.69 mM (CI_{95} = 0.78 to 2.60) (Fig. 2C). The change in oxygen concentration as a function of the initial ratio of oxygen to methane in the culture headspace (i.e., oxygen-to-methane headspace ratio; slope of the oxygen curve) was greater than the change in the methane concentration (i.e., slope of the methane curve) (Fig. 2D), suggesting that the effects of the initial availability of oxygen and methane on the respective proportions

of both substrates were mainly mediated by higher oxygen consumption (Fig. 2D). The specific uptake rate of oxygen tended to be higher than that of methane under all experimental conditions except the culture containing the lowest initial oxygen headspace percentage (Fig. 2E). In the cultures with initial oxygen headspace percentages ranging from 10% to 25%, the ratio between the specific uptake rates of oxygen and methane remained similar (1.2:1 to 1.4:1), while the ratios between the changes in the concentrations of oxygen and methane varied from 0.75:1 to 1.3:1 (Fig. 2F). Interestingly, only the culture with the lowest initial oxygen headspace percentage had a low ratio (~0.5:1) between the specific uptake rates of oxygen and methane (Fig. 2F) and a noticeably lower rate of specific growth (Fig. 2C).

Features of the GEM of *M. album* BG8. Given the strong effect of the initial oxygen headspace percentage on the growth rate and metabolic yields, we next aimed to elucidate the metabolic states induced by different levels of oxygen availability in *M. album* BG8. To achieve a system-level understanding of *M. album* BG8 metabolism, we constructed a high-quality GEM that incorporated all of the central metabolic pathways contributing to methane oxidation (Fig. 3) and many other pathways that provide energy (ATP is produced by aerobic respiration through oxidative phosphorylation) and precursors for biomass production in *M. album* BG8 (Fig. 4). The final GEM was established after manually curating the gene-protein-reaction (GPR) associations and biomass compositions in the draft model generated by KBase (43), which led to the addition of 16 genes, 33 metabolites, and 181 reactions. The final curated GEM comprises 803 genes, 1,367 metabolites, and 1,358 reactions (Fig. 4A), uses the nutrient parameters described in Materials and Methods, and constrains only methane and oxygen uptake fluxes by default (Fig. 4B). The differences in metabolic reactions between the draft and curated versions of the model are detailed in Table S2. Although the final model does not seem underdetermined at steady state (more metabolites than reactions), many metabolites in the model are not directly involved in FBA solutions to maximize the biomass production reaction (e.g., only ~550 metabolites were involved at an oxygen flux of 15 mmol/gDCW/h and a variable methane uptake flux). Furthermore, the final model purposely includes five blocked reactions (i.e., flux is not allowed) (Fig. 4C), of which four are involved in alternative biomass production (containing different growth-associated ATP maintenance assumptions) and one involves an alternative methanol dehydrogenase, and 171 orphan reactions (i.e., with no GPR associations) that were added through the automatic gap-filling of the draft GEM. Among the orphan reactions, 72 are exchange reactions required to interact with the external compartment of the model, and the rest are required to sustain biomass production in the model. However, homologs for their GPR associations could not be detected through genome (re)annotation.

By applying the FBA (44) and minimization of metabolic adjustment (MOMA; linearized version) (45) approaches to the model simulations, 281 essential genes were identified in which a single *in silico* gene knockout resulted in growth inhibition (Fig. 4D). Consequently, the high-quality final version of the *i*JV803 GEM included 45 metabolic pathways containing more than five reactions (Fig. 4E). In descending order, (i) the glycerophospholipid metabolism, (ii) fatty acid metabolism, (iii) exchange/demand and transport reactions, (iv) nucleotide interconversion, and (v) cell wall biosynthesis pathways contained the largest numbers of reactions (Fig. 4E). However, reactions that cannot be assigned to specific metabolic pathways accounted for a large proportion of the total reactions, and these remain to be classified in future studies (Fig. 4E).

Metabolic modeling capabilities of the GEM of *M. album* BG8. We next tested the modeling capabilities of the GEM for *M. album* BG8 using FBA. We first evaluated the growth rate obtained in the FBA based solely on the experimentally derived methane specific uptake rates. The lower and upper 99% CIs of the methane specific uptake rates derived from cultures with different initial oxygen-to-methane headspace ratios (Fig. 2E) were used as the uptake flux constraint. As shown in Fig. 5A, the growth rates in the FBA were similar to the experimental results, demonstrating the accuracy of the GEM. We also evaluated the ratio obtained in the FBA between the oxygen and methane specific uptake rates that would maximize the growth rate and found that the flux

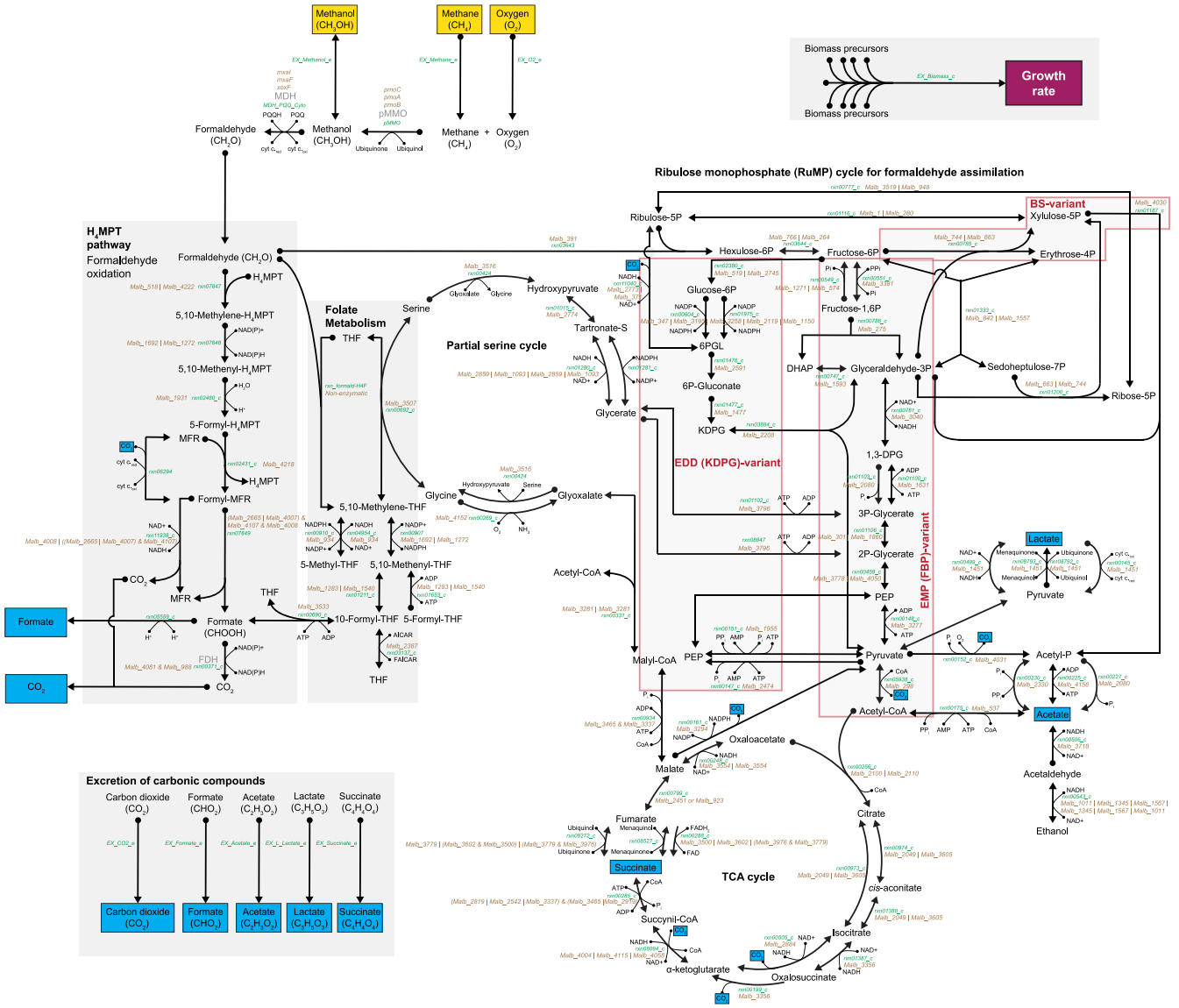

FIG 3 Central methanotrophic metabolic pathways in *Methylomicrobium album* BG8. Metabolites that are taken up are highlighted in yellow, and those excreted are labeled in blue. Metabolite names are shown in black, reaction identification numbers are in green, and the genes associated with each reaction are in brown. The pathway names are boldfaced. The chemical formula describing the key metabolites involved in the initial methane oxidation and the consumed and excreted metabolites is shown. Nonreversible and reversible reactions, determined according to the thermodynamics constraints of every reaction, are indicated by single-headed and double-headed arrows, respectively. Abbreviation of the pathway names: H_4MPT, tetrahydromethanopterin; EDD (KDPG), Entner-Doudoroff Pathway (2-keto-3-deoxy-6-phosphogluconate aldolase); EMP (FBP), Embden-Meyerhof-Parnas (fructose 1,6-bisphosphatase); BS, *Bifidobacterium* shunt; TCA, tricarboxylic acid.

ratio of ~1.5:1 matched the specific uptake rate ratios observed in the cultures with a higher initial oxygen headspace percentage (Fig. 5B).

In the same experiment (Fig. 2), the initial oxygen-to-methane headspace ratio and the specific oxygen and methane uptake rates strongly influenced the growth rates and the final excreted metabolite yields and concentrations. To investigate the variations in growth rate under different oxygen-to-methane uptake flux ratios, a phenotype phase plane analysis was performed while controlling the oxygen and methane uptake flux reactions and maximizing the biomass production reaction (Fig. 5C). Consistent with the experimental results (Fig. 2), the GEM showed a range of ratios of oxygen-to-methane uptake flux within which growth was feasible (above the line showing slope of 1 in Fig. 5C). The highest growth rate was obtained in the FBA at a slope of ~1.5 (Fig. 5C), indicating that although biomass production is possible at an oxygen-to-methane uptake flux ratio slightly greater than 1:1, the ideal oxygen uptake flux is ~1.5 times that of

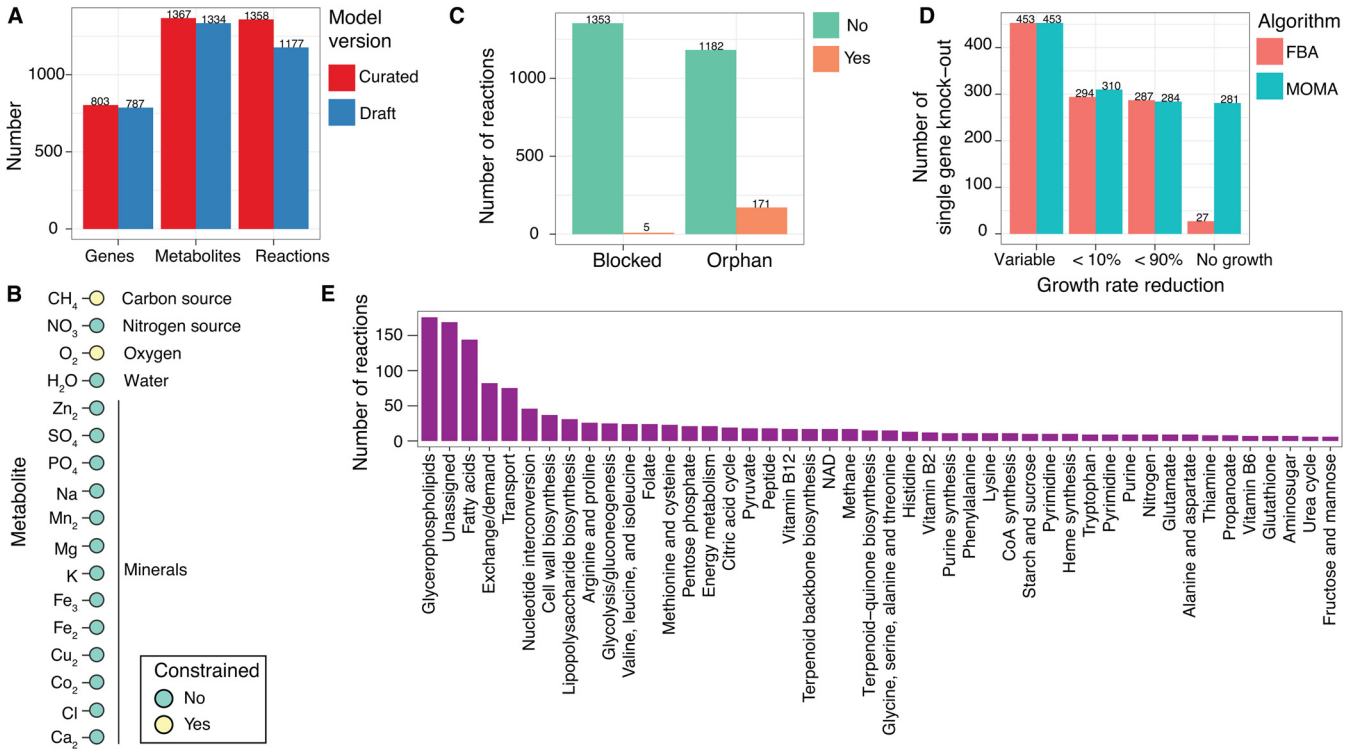

FIG 4 Features of the genome-scale metabolic model (GEM) of *Methylomicrobium album* BG8. (A) Comparison of the key features between the draft and curated models. (B) The default *in silico* medium composition used in the GEM. Only the methane and oxygen uptake fluxes were constrained by default. (C) Numbers of blocked and orphan reactions included in the curated model. (D) Effects of *in silico* single-gene knockouts on the growth rate. (E) Numbers of reactions in each pathway. Pathways with fewer than five reactions have been omitted to enhance visualization.

methane (Fig. 5C). Interestingly, most of the experimentally determined specific uptake rate ratios (Fig. 2F) were within the range of feasible growth obtained in the FBA; the experiment with the lowest initial oxygen headspace percentage (5%) was the only exception (Fig. 5C). This result suggests that the specific oxygen and methane uptake rates are not optimal for *M. album* BG8 growth when oxygen availability is very low.

GEM revealed the role of oxygen availability in balancing formaldehyde oxidization and assimilation. Given the apparent effect of oxygen on methane oxidation and subsequent biomass production and metabolite excretion (Fig. 2), the GEM was used to further investigate the effects of oxygen on system-level metabolism in *M. album* BG8. Using time-series data from the experiments conducted under various initial oxygen headspace percentages (Fig. 2), the growth rates, methane and oxygen uptake fluxes, and carbon dioxide, formate, and acetate excretion fluxes in the exponential phase were computed (Fig. 5D). The mean growth rate increased with the initial oxygen headspace percentage (Fig. 5D). The methane and oxygen uptake fluxes and carbon dioxide excretion flux were significantly different in the culture with the lowest oxygen-to-methane headspace ratio compared to the rest (Fig. 5D). Similar to the experimental results obtained for yields (Fig. S2), no clear positive associations were observed between the formate excretion fluxes and the initial oxygen headspace percentage in the model (Fig. 5D). Nevertheless, the experiment with the highest initial oxygen-to-methane headspace ratio exhibited the highest formate excretion flux (Fig. 5D). Acetate flux was only detected in the culture with the lowest initial oxygen-to-methane headspace ratio (although the concentration was low and the uncertainty was high; Fig. 5D).

The use of the upper and lower bounds of the measured fluxes as constraints on the respective reactions in the GEM enabled the construction of a parametrized GEM for each experimental condition. Subsequently, the distribution of flux in the key central metabolic pathways was analyzed in detail (Fig. 5E to G). The parametrized GEM revealed significant

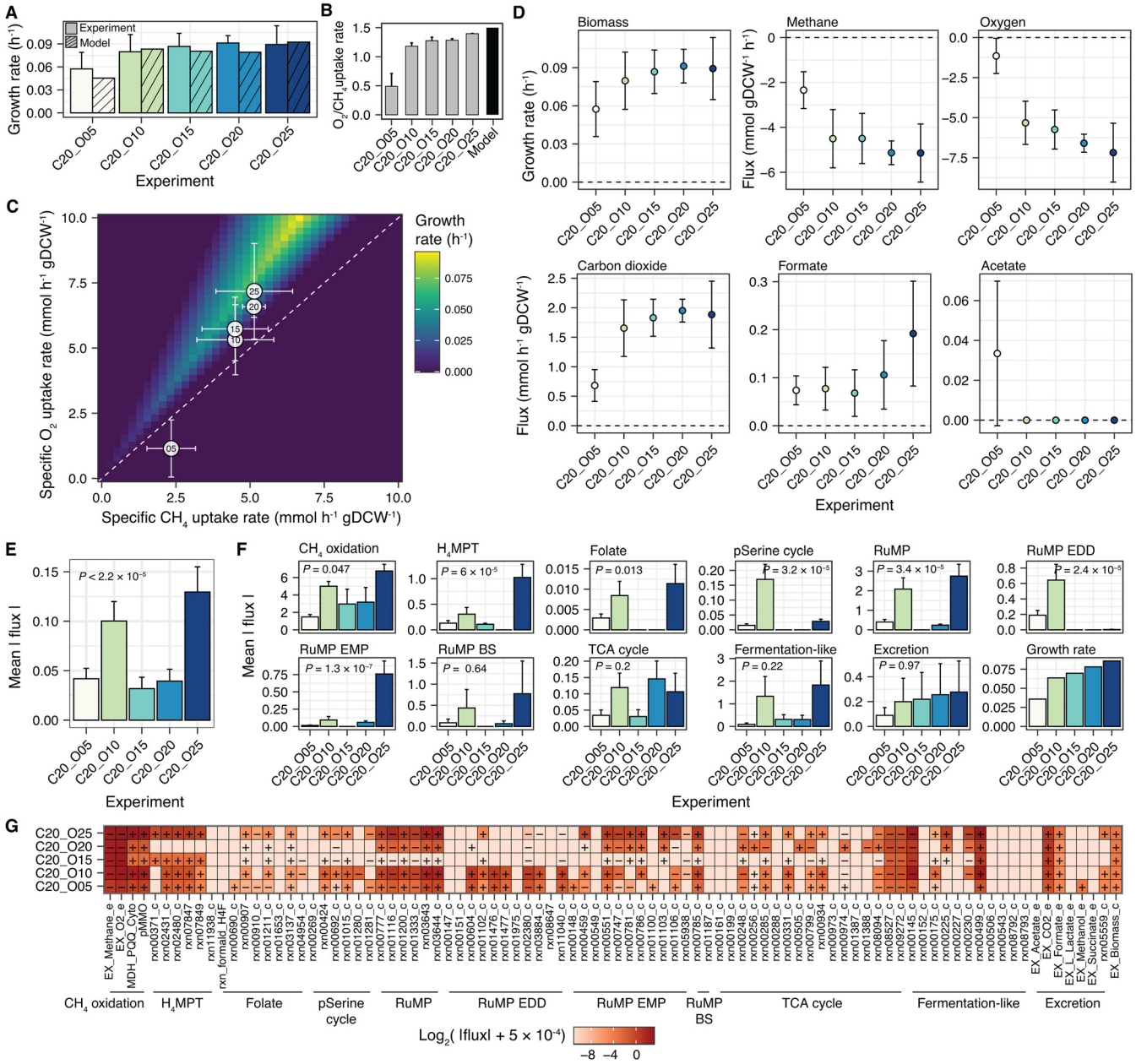

FIG 5 Metabolic modeling capabilities of the genome-scale metabolic model (GEM) of *Methylomicrobium album* BG8 and construction of parametrized GEMs under different initial percentages of oxygen (5% to 25%) in 5% increments with 20% methane. (A) Comparison of the experimental and FBA growth rates. Error bars on the experimental data represent the 99% confidence intervals. (B) Comparison of the experimental specific uptake rate ratios with the FBA optimal oxygen-to-methane uptake flux ratios. (C) Phenotype phase plane analysis of the growth rates at different oxygen-to-methane uptake flux ratios. The white circles denote the experimentally determined specific uptake rates, and the error bars represent the 99% confidence intervals. The number inside each circle indicates the initial oxygen headspace percentage in each experiment. (D) Experimentally determined growth rate and fluxes; the error bars represent the 99% confidence intervals, indicating accuracy of the sample mean estimator. (E) Mean absolute flux throughout the metabolic network in the parametrized GEM of each experiment. (F) Mean absolute flux of each central metabolic pathway indicated in Fig. 3. For panels E and F, the mean values of the fluxes are shown, the error bars represent the standard errors, and the *P* values were calculated using the Kruskal-Wallis test. (G) Heatmap of the flux through each reaction in the central metabolic pathways. The plus and minus symbols denote the directions of the reactions in the biochemical network. For each reaction mix, 5×10^{-4} mmol h^{-1} $gDCW^{-1}$ was added to the absolute flux value to avoid zero flux and enable visualization of the flux values on a $\log_2$ scale.

differences in mean flux between the five oxygen conditions (*t* test, $P < 0.05$) (Fig. 5E), with the highest values obtained in the cultures with initial oxygen headspace percentages of 25% and 10% (Fig. 5E). Significant differences (*t* test, $P < 0.05$) were observed in the methane oxidation pathway, the H_4MPT pathway, the folate metabolism, the partial serine cycle, the RuMP cycle, the RuMP EDD variant, and the RuMP EMP variant (Fig. 5F). Notable formaldehyde dehydrogenase (FDH, rxn00371_c) (Fig. 3) activity was detected in

the experiments initially provided with 15% and 25% oxygen (Fig. 5G), while the NADH-consuming glycerate production reaction (rxn01280_c) (Fig. 3) was only highly active in the culture initially provided with 10% oxygen (Fig. 5G).

Overall, the results of the parametrized GEM-based system-level analysis of *M. album* BG8 cultures provided with different initial oxygen headspace percentages reveal that these cultures differ mainly in the regulation of formaldehyde oxidization and assimilation. At an initial oxygen-to-methane headspace ratio of 1.25:1, formaldehyde can be efficiently oxidized through the H_4MPT pathway and assimilated mainly through the RuMP cycle and its EMP variant (Fig. 3 and 5F and G). However, at an initial oxygen-to-methane headspace ratio of $<$0.75:1, the folate metabolism pathway contributes to the oxidation of formaldehyde, which is then assimilated through the EDD variant of the RuMP cycle (Fig. 3 and 5F and G). Interestingly, the FBA showed that some methanol must be excreted to perform efficient methane oxidation under the condition of low initial oxygen availability (5%) (Fig. 5G). Furthermore, the FBA showed that the culture with the highest biomass yield (20% methane and 20% oxygen) carried a relatively lower mean absolute flux through its metabolic network (Fig. 5E) and high activity throughout the tricarboxylic acid (TCA) cycle (Fig. 3 and 5G).

Regulation of organic compound excretion by the oxygen-to-methane uptake flux ratio. Because the initial oxygen headspace percentage had a system-level effect on the metabolic state of *M. album* BG8, a potential mechanistic link to organic compound excretion and biomass production was further investigated. Because the GEM cannot account for absolute concentrations, we focused our analysis on the oxygen-to-methane uptake flux ratio. The GEM was used to perform over 700 simulations in which the lower and upper bounds of the methane uptake flux were set to an arbitrary value of 10 mmol h^{-1} $gDCW^{-1}$ and the lower and upper bounds of the oxygen uptake flux were set to be the same and allowed to vary from 0 to 30 mmol h^{-1} $gDCW^{-1}$. The large volume of simulation results provided insight into the effects of different combinations of methane and oxygen uptake fluxes on the production of biomass and ATP and the excretion of organic compounds, including carbon dioxide, formate, acetate, lactate, and succinate.

The FBA showed that oxygen-to-methane uptake flux ratios in the range of $>$0:1 to $<$2.5:1 were feasible to support biomass and ATP production (Fig. 6A) and organic compound excretion (Fig. 6B). The optimal ratio for biomass and ATP production was $\sim$1.5:1 (Fig. 6A). At high ($>$2:1) oxygen-to-methane uptake flux ratios, carbon dioxide and formate were preferentially excreted (Fig. 6B), consistent with the experimental results measured in the exponential growth phase (Fig. 1A and 2A). By limiting the analysis to excreted metabolites that could be experimentally detected (i.e., carbon dioxide, formate, and acetate), the simulation demonstrated that when the oxygen uptake flux decreased (i.e., a lower oxygen-to-methane uptake flux ratio), formate and (eventually) acetate accounted for a larger fraction of the total excreted flux, whereas the carbon dioxide excretion flux was reduced (Fig. 6C). These results are consistent with the experimental phenotypes measured during the late-exponential and stationary phases (Fig. 1A and 2A).

Metabolic modeling of a high-acetate-excreting phenotype identified a mixed mode involving both respiration and fermentation. Studies (46–50) have determined that the initial biomass concentration can affect microbial growth and metabolic capabilities. Here, we further investigated the effects of two relatively different initial biomass concentrations (low and high) on system-level metabolism in *M. album* BG8. Both biomass concentrations were tested under the initial oxygen-to-methane headspace ratios that promoted the highest biomass and organic compound excretion yields (1:1 [20% methane and 20% oxygen] and 1.25:1 [20% methane and 25% oxygen]). Under both ratios, the initial biomass concentration had a significant ($P < 0.05$) and specific effect on the formate and acetate yields (Fig. 7A). In the cultures with a lower initial biomass concentration, a higher formate yield was achieved under the 1:1 oxygen-to-methane headspace ratio compared with the 1.25:1 ratio (Fig. 7A). However,

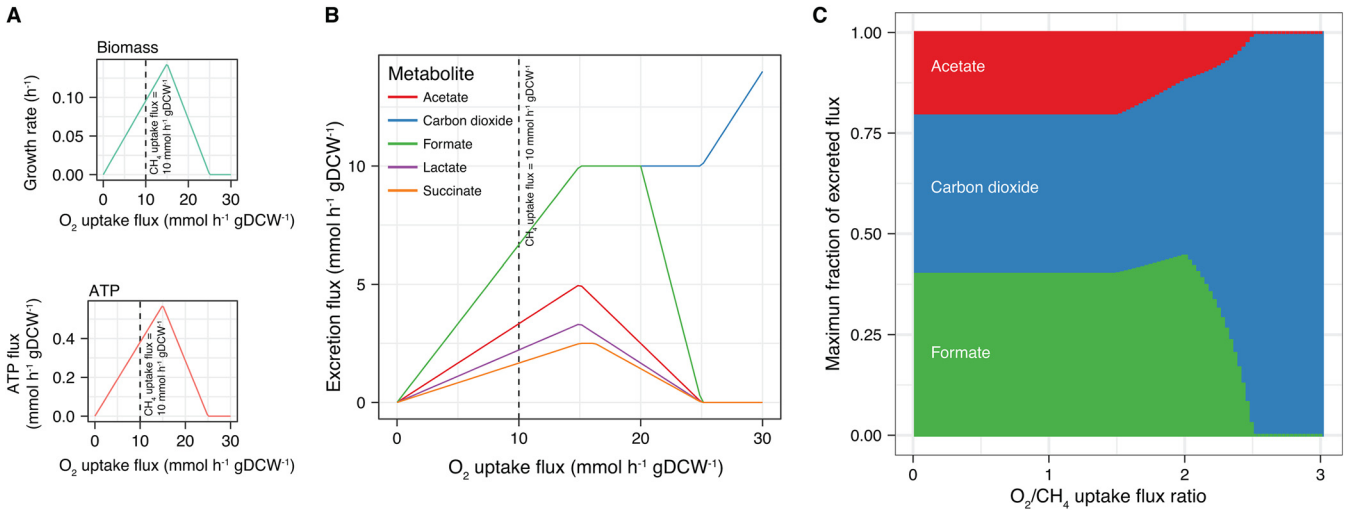

FIG 6 Modeled effects of the oxygen-to-methane uptake flux ratio on metabolism in *Methylomicrobium album* BG8. Effects of variations in the oxygen uptake flux on the growth rate, ATP generation (A), and organic compound excretion(B). Each metabolite was analyzed separately, and the excretion reaction of each was set as the objective function in the FBA. For panel B, the carbon dioxide and formate lines partially overlap. (C) Analysis of the maximum fractions of excreted flux for the three metabolites detected experimentally at different oxygen-to-methane uptake flux ratios. A constant methane uptake flux of 10 mmol h^{-1} $gDCW^{-1}$ was used in all of the analyses.

the acetate yield was higher in the cultures with a relatively higher initial biomass concentration under both oxygen-to-methane headspace ratios (Fig. 7A).

No consistent trends in the methane and oxygen uptake fluxes were observed between the cultures with high and low initial biomass concentrations grown under different initial oxygen-to-methane headspace ratios (Fig. 7B). Furthermore, the biomass concentration had a significant effect on formate and acetate excretion (Fig. 7B, the accuracy of the sample mean estimator was determined by the 99% confidence intervals represented by the error bars) but not on carbon dioxide excretion. Acetate excretion flux was observed during the exponential phase under a relatively higher initial biomass concentration and an initial oxygen-to-methane headspace ratio of 1:1 (Fig. 7B). However, these conditions led to a significantly lower growth rate than those of the other three cultures (Fig. 7B).

Although the effects of changing the initial biomass concentration in the experiments cannot be directly simulated using FBA, we approached the metabolic effects of different initial biomass concentrations by constraining the GEM with the experimentally measured growth rates, uptakes of methane and oxygen, and excretion of carbon dioxide, formate, and acetate of the different cultures. The parametrized GEMs were then used to model the metabolism of *M. album* BG8, revealing that only the culture with a relatively higher initial biomass concentration and an initial oxygen-to-methane headspace ratio of 1:1 exhibited significantly higher (*t* test, $P < 0.05$) mean absolute fluxes in the overall metabolic network (Fig. 7C) and in several metabolic pathways, including H_4MPT, folate metabolism, the partial serine cycle, RuMP cycle, the EMP variant of the RuMP cycle, and the tricarboxylic acid (TCA) cycle (Fig. 7D). In the cultures grown under an initial oxygen-to-methane headspace ratio of 1.25:1, we identified significant effects of the initial biomass concentration ($P < 0.05$) on the mean absolute fluxes in the metabolic pathways of H_4MPT and the EMP and EDD variants of the RuMP cycle (Fig. 7D).

A detailed analysis of affected pathways and reactions in the acetate-excreting phenotype indicated that the BS variant of the RuMP cycle, the reactions of which are linked to fermentation-like reactions, exhibited a high level of flux (Fig. 7E). In fact, high levels of flux (Fig. 7E) were observed in the reaction that converts fructose-6P plus glyceraldehyde-3P to xylulose-5P and erythrose-4P (rxn00785_c) and the subsequent reaction that converts xylulose-5P to acetyl-P (rxn01187_c) (Fig. 3). Acetyl-P and acetate can be interconverted through the reactions rxn00230_c and rxn00225_c (with ATP generation), both of which exhibited high levels of flux in this phenotype (Fig. 7E).

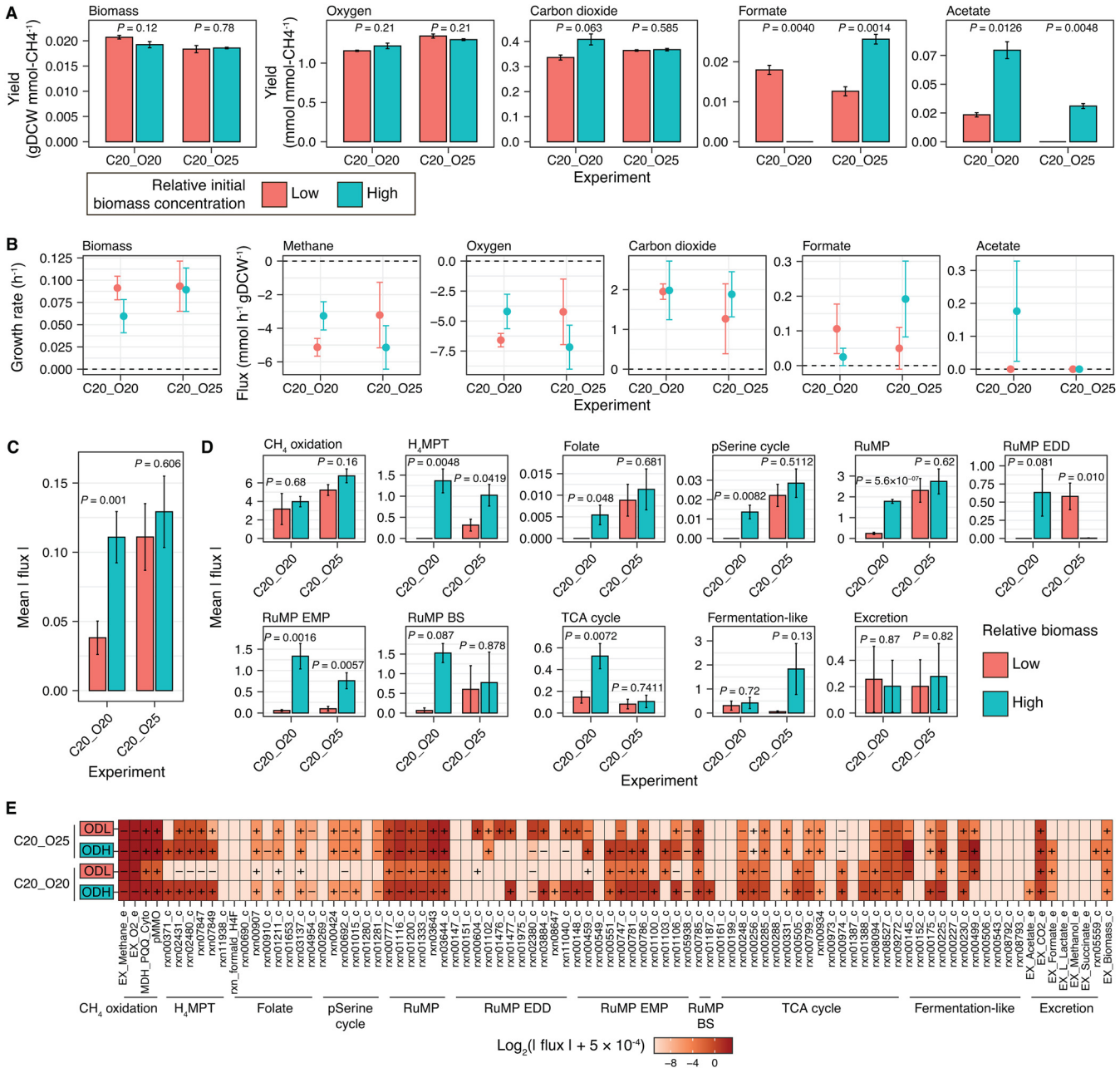

FIG 7 Effects of the initial biomass concentration on metabolism in *Methylomicrobium album* BG8 under two initial oxygen-to-methane headspace ratios (20% methane and 20% oxygen; 20% methane and 25% oxygen). (A) Biomass, oxygen uptake, and excreted metabolite yields. The data are shown as mean values of biological triplicates, and the error bars represent the standard errors. (B) Experimentally determined flux values; the error bars represent the 99% confidence intervals. (C) The mean absolute flux throughout the metabolic network in the parametrized genome-scale metabolic model of each experiment. (D) The mean absolute flux in each central metabolic pathway indicated in Fig. 3. For panels C and D, the mean values of the fluxes are shown, the error bars represent the standard errors, and the *P* values were calculated using the two-sided *t* test. (E) Heatmap of the flux through each reaction in the central metabolic pathways. ODL and ODH represent low and high relative initial biomass concentrations, respectively. The plus and minus symbols denote the directions of the reactions in the biochemical network. In each reaction mixture, a value of 5×10^{-4} mmol h^{-1} $gDCW^{-1}$ was added to the absolute flux value to avoid a zero flux and facilitate visualization of the flux values on a $\log_2$ scale.

Furthermore, the parametrized GEM of this acetate-excreting phenotype indicated a second pathway leading to acetate excretion. Specifically, high flux was observed in the pathway that converts pyruvate to acetyl-coenzyme A (CoA) (rxn05938_c) and acetyl-CoA to acetate (rxn00175_c) (Fig. 3 and 7E) and also generates ATP (Fig. 3). Intriguingly, the reactions that convert malate to malyl-CoA (rxn00934, Fig. 3) and malyl-CoA to acetyl-CoA plus glyoxalate (rxn00331_c) (Fig. 3) both exhibited high levels of flux, suggesting that this pathway replenishes acetyl-CoA at the expense of ATP

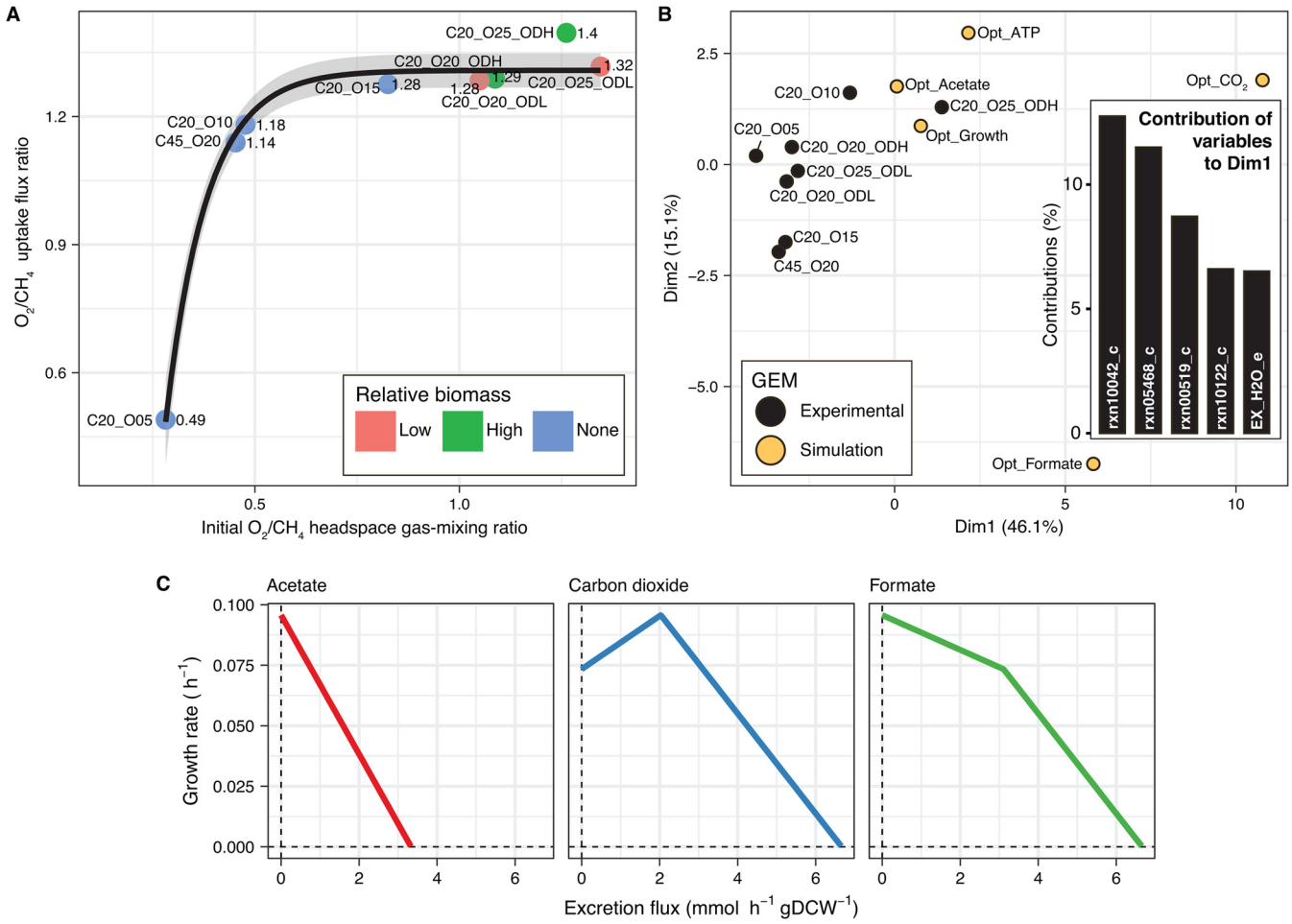

FIG 8 Metabolic versatility of and metabolic couplings in *Methylomicrobium album* BG8. (A) The oxygen-to-methane uptake flux ratio as a function of the initial oxygen-to-methane headspace ratio under all of the experimental conditions. A bounded exponential model was fitted to the data; the gray-shaded region represents the 95% confidence interval. (B) Results of a principal-component analysis (PCA) of the overall metabolic flux in each experimental culture. Five simulated constrained models were included in the PCA to represent phenotypes optimized for growth, ATP generation, carbon dioxide production, formate excretion, or acetate excretion. The top 5 reactions that contributed the most to the ordination of the phenotypes based on the loadings in dimension 1 of the PCA are shown in the inset. (C) Multiple FBA wherein the acetate, carbon dioxide, or formate excretion reaction was controlled and the biomass production reaction was maximized. The lines indicate the coupling between the rate of growth and the excretion flux of a metabolite. Five hundred simulations were performed for each metabolite.

and connects the TCA cycle with the partial serine cycle. In turn, the active production of malate and subsequent generation of acetyl-CoA would explain the high flux in the TCA cycle in this phenotype (Fig. 7E). Interestingly, the flux analysis of this acetate-excreting phenotype also revealed that the entire TCA cycle was used to produce one molecule of ATP, three molecules of NADH, and one molecule of ubiquinol and to excrete carbon dioxide (Fig. 3 and 7E). Taken together, the results of integrative modeling in this study suggest that the high acetate-excreting phenotype uses a mixed metabolic mode in which the pathways required for respiration and fermentation are simultaneously active.

Metabolic versatility of *M. album* BG8 and coupling between biomass production and organic compound excretion. After separately analyzing and describing the effects of the initial methane (Fig. 1), oxygen (Fig. 2), and biomass (Fig. 7) concentrations on the metabolism of *M. album* BG8, we quantitatively investigated the associations of these factors with the oxygen-to-methane uptake flux ratio, an important parameter used to define phenotypes (Fig. 6). In all of the experiments, the relationship between the initial oxygen-to-methane headspace ratio and the calculated oxygen-to-methane uptake flux ratio could be described using a bounded exponential model (Fig. 8A). At an initial oxygen-to-methane headspace ratio of >0.5:1, the maximum oxygen-to-methane uptake

flux ratio was 1.3:1 to 1.4:1 (Fig. 8A), consistent with the FBA result of an optimal oxygen-to-methane uptake flux ratio of ~1.5:1 for growth and ATP generation (Fig. 6A).

A PCA was applied to the results of the parametrized GEM to compare the metabolic flux between different cultures (Fig. 8B). Based on the results, most of the experimental phenotypes were clustered together, except the phenotype grown under 20% methane, 25% oxygen, and a relatively high biomass (C20_O25_ODH) (Fig. 8B). Interestingly, this phenotype also yielded an oxygen-to-methane uptake flux ratio of 1.4:1 (the highest observed in all our cultures), which deviated from the confidence interval of the bounded exponential model (Fig. 8A). Cultures with different methane and oxygen headspace percentages but similar initial oxygen-to-methane headspace ratios also had similar oxygen-to-methane uptake flux ratios (Fig. 8A) but slightly different metabolic fluxes, as indicated by their separation on the PCA plot (Fig. 8B).

The results of GEM simulations of phenotypes optimized for growth, ATP generation, or carbon dioxide, formate, and acetate excretion were also included in the PCA as reference values (Fig. 8B). Although the metabolic fluxes resulting from the FBA tended to differ between the experimental cultures, these values were relatively closer to the reference phenotypes optimized for growth, acetate excretion, and ATP generation and clearly distant from the phenotypes optimized for carbon dioxide and formate excretion (Fig. 8B). This metabolic versatility may have enabled *M. album* BG8 to optimize for growth and ATP generation under different conditions by using different pathways. A closer examination of the top five reactions that contributed the most to the ordination of the phenotypes, based on the loadings in dimension 1 of the PCA (inset in Fig. 8B), revealed that reactions involved in energy generation (rxn10042_c, ATP synthase; rxn05468_c, oxygen transport via diffusion; rxn00519_c, oxaloacetate carboxy-lyase; rxn10122_c, NADH dehydrogenase; and EX_H2O_e, water exchange) were most relevant to define the phenotypes.

An analysis of the metabolic fluxes in the optimal phenotype for acetate production revealed a cluster that included the phenotypes optimized for growth and ATP generation and the phenotypes indicated by the FBA of the experimental cultures. Acetate may be a highly relevant metabolite that balances the pathways contributing to energy and biomass production in *M. album* BG8. In fact, we hypothesized that a trade-off existed between biomass production and acetate excretion in this strain. This hypothesis was partially supported by the observation of a reduction in the growth rate when acetate was excreted during the exponential phase (Fig. 7B).

To test our hypothesis, we applied multiple FBA in which the acetate excretion reaction was controlled and the biomass production reaction was maximized. The lower and upper bounds of both the methane and oxygen uptake fluxes were set to -10 mmol h^{-1} $gDCW^{-1}$ and 0 mmol h^{-1} $gDCW^{-1}$, respectively. This enabled the GEM to automatically adjust the oxygen-to-methane uptake flux ratio to maximize the growth rate under every acetate excretion condition. Consistent with the hypothesis, the multiple FBA revealed a trade-off between the biomass production and acetate and formate excretion (Fig. 8C) and a coupling between biomass production and carbon dioxide excretion (Fig. 8C). In fact, a carbon dioxide excretion flux between 0 and 2 mmol h^{-1} $gDCW^{-1}$ (Fig. 8C), which matched the experimentally measured range, favored the growth rate (Fig. 5D and 7B).

DISCUSSION

The aim of this study was to elucidate the system-level metabolism of *M. album* BG8 using an integrative systems biology framework. The integration of time-series growth and compound uptake and excretion data into a newly developed, high-quality GEM yielded novel insights into the metabolic mechanisms of this methanotrophic bacterial strain. Furthermore, the experimental data collected in this study enabled the construction of parametrized GEMs, and the application of an FBA enabled the system-level understanding of the metabolism of *M. album* BG8 under different initial concentrations of oxygen, methane, and biomass.

The conversion factor of 0.26 gDCW liter^{-1} derived between the OD_{600} and DCW of *M. album* BG8 in our study differs from a previously reported conversion factor of 0.33 gDCW liter^{-1} (51). Although a linear regression of our data with a *y* intercept of −0.044 yielded a conversion factor of 0.32 gDCW liter^{-1} (see Fig. S1 in the supplemental material), this model was not used due to a lower adjusted R^2 and a less significant *P* value than those of our selected model. These results highlight the need for caution regarding potential variability in the conversion factor between OD_{600} and DCW when studying *M. album* BG8. However, the Monod model was used to estimate growth kinetics as a function of the initial oxygen headspace percentage, and the calculated μ_{max} value (0.11 h^{-1}) is similar to other reported growth rates for *M. album* BG8 (e.g., 0.10 h^{-1} to 0.18 h^{-1} with different concentrations of methane [24, 51], 0.09 h^{-1} to 0.13 h^{-1} with different concentrations of chloromethane [52], and 0.11 h^{-1} with methanol [53]). However, the Monod model assumed that oxygen was the only limiting substrate, which may not be true in a real-life scenario.

We identified oxygen as the key driver of methane oxidation by *M. album* BG8, as it exerted strong effects on both biomass production and organic compound excretion. In our analysis, optimal growth could be sustained at a ratio of ~1.5:1 between the specific uptake rates of oxygen and methane. In agreement with our results, a ratio of ~1.5:1 between oxygen and methane uptake rates has also been found by FBA to be optimal for growth for the methanotroph *Methylomicrobium buryatense* 5GB1 after careful correction of pathways in the GEM (54). Biomass production was maximized under culture conditions of 20% methane and 20% oxygen, with a yield of 0.021 gDCW mmol-CH_4^{-1}. This was the only culture indicated by the parametrized GEM to have a completely active TCA cycle and to exhibit a low mean level of absolute flux throughout its metabolic network. We speculate that these results of integrative *M. album* BG8 modeling indicate an optimal methanotrophic state for the allocation of molecular and metabolic resources in which optimal biomass production is preserved and enzyme use is minimized. Future work is required to further explore this notion. These results also complement the findings of recent work in which *M. album* BG8 was identified as the bacterium with the highest biomass yield (nearly double that of the others tested) among a group of industrially relevant methanotrophs (25).

Intriguingly, the GEM showed the excretion of methanol as a by-product of growth under the condition with the lowest initial oxygen availability (5%). The GEM was parametrized (based on the experimental data) with an uptake rate bounded at 1.52 to 3.16 mmol h^{-1} gDCW^{-1} for methane and an uptake rate bounded at 0.05 to 2.24 mmol h^{-1} gDCW^{-1} for oxygen. A possible explanation for this methanol-excreting phenotype from the FBA is that methanol works as an additional control for the metabolic branching at low oxygen concentrations, leading to tetrahydrofuran-based oxidation of formaldehyde in addition to metabolic flux through the EDD variant of the RuMP cycle and partial serine pathways. Hence, instead of actual methanol release to the extracellular environment (which was not detected in the medium), *M. album* BG8 could be using the mentioned pathways to more efficiently oxidize methanol to gain biomass. A recent transcriptomics and metabolomics study of *M. album* BG8 grown on methanol (55) yielded a phenotype that is similar to the condition with low availability of oxygen. Increased transcription of genes related to carbon metabolism through the RuMP EDD variant and pentose phosphate pathways as well as formaldehyde detoxification through the glutathione dependent pathway, of which formate is the product, were observed (55). Taking the reported transcriptomics and metabolomics data (55) together with the GEM and FBA results presented here, they suggest that *M. album* BG8 favors methanol oxidation over methane as oxygen availability diminishes.

Although carbon dioxide and formate are usually excreted during aerobic methanotrophy (27), these metabolites have recently become valuable by-products (56, 57) and are used as carbon sources in synthetically constructed methanotrophic modular microbial consortia to produce value-added compounds (58). In our study, the highest carbon dioxide yield (0.39 mmol mmol-CH_4^{-1}) was achieved under culture conditions of

20% methane and 20% oxygen, and the highest formate yield (0.025 mmol mmol-CH_4^{-1}) was obtained under conditions of 20% methane and 25% oxygen. In contrast to a recent report (25), formate excretion was detected in all of the cultures in this study. The phenotype with the highest formate yield exhibited the highest mean absolute flux through its metabolic network and the second highest flux through the H_4MPT formaldehyde oxidation pathway. In other words, by actively using the complete H_4MPT pathway, this phenotype can generate two reducing equivalents [NAD(P)H]. Based on these results, developers of metabolic engineering strategies that aim to optimize carbon dioxide and/or formate excretion by *M. album* BG8 during methane metabolism may consider directing carbon flux toward the H_4MPT pathway. Nevertheless, future attempts to optimize formate production by *M. album* BG8 should consider the achievement of significantly larger formate yields by other methanotrophs grown on methanol instead of methane (59–61). Although a previous study investigated the effects of methane and methanol on formate excretion by *M. album* BG8, the authors did not detect formate under the tested conditions (25), likely because the samples collected in the reported experiments corresponded to the early stages of *M. album* BG8 growth in our experimental setup.

Acetate is a key precursor in high-value chemical production (62). Therefore, the biotechnological potential of *M. album* BG8 in the conversion of methane to valuable compounds depends on the ability to produce a high acetate yield. Among the different culture conditions in this study, the highest acetate yield (0.072 mmol mmol-CH_4^{-1}) was unexpectedly obtained under the conditions of 20% methane, 20% oxygen, and a relatively high initial biomass concentration (Fig. 7A). This culture of *M. album* BG8 excreted acetate during the exponential phase (Fig. S3) but resulted in a relatively lower growth rate at this phase (Fig. 7B), indicating a trade-off between biomass production and acetate excretion (Fig. 7) that was further supported by the model FBA (Fig. 8C). However, the molecular and metabolic mechanisms behind this trade-off remain unclear and need to be further investigated. Previous reports have described acetate excretion by other gammaproteobacterial methanotrophs under prolonged oxygen starvation (63) and oxygen-limited growth (64). Our experimental results agree with those findings, as acetate excretion was detected in all cultures in which oxygen was present at a very low concentration or completely depleted. Similarly, the FBA showed a high acetate excretion flux in *M. album* BG8 at a low ($<$1.5:1) oxygen-to-methane uptake flux ratio (Fig. 6C). Overall, we expect that the metabolic characterization of acetate excretion presented here will support future attempts to increase acetate yields and achieve the metabolic reprogramming of acetyl-CoA conversion in *M. album* BG8.

Both the oxygen-to-methane headspace ratio and specific uptake ratio have been explored intensively in methanotrophy studies (59, 63, 65–68), as these variables are thought to control the differential activation of pathways required for the production of biomass, generation of energy, and induction of fermentation-like metabolism (63, 64). The *M. album* BG8 genome encodes homologs of enzymes found in the EDD and EMP RuMP cycle variants in *M. alcaliphilum* 20Z and *M. buryatense* 5G(B1) (64). However, *M. album* BG8 lacks 3 of the 18 key enzymes [i.e., phosphate acetyltransferase, D-fructose 6-phosphate phosphoketolase, and NAD(P)-dependent malic enzyme] required for fermentation-like metabolism in *M. alcaliphilum* 20Z (64) and *M. buryatense* 5G(B1) (63) at low oxygen-to-methane concentration ratios. Nevertheless, the *M. album* BG8 cultures exhibited a fermentation-like metabolism with high acetate excretion and low carbon dioxide and formate excretion mainly during the stationary phase when the oxygen-to-methane concentration ratio was very low. However, in terms of energetic investigations with the current version of the GEM, it is important to note that the growth-associated and non-growth-associated ATP maintenance have not been specifically determined for *M. album* BG8. Thus, future work is required to experimentally determine these parameters for *M. album* BG8, as has been described elsewhere (69, 70). Finally, we identified a nonlinear relationship between the initial oxygen-to-methane headspace ratio and the oxygen-to-

methane uptake flux ratio in batch cultures of *M. album* BG8, which will facilitate control of the oxygen-to-methane uptake flux ratio in batch systems.

In summary, the experimental results and the FBA presented in this study elucidate some of the characteristics of *M. album* BG8. However, many other aspects of metabolism in this strain remain to be explored in detail. The newly developed GEM of *M. album* BG8 is a valuable tool that will aid future investigations of this important methanotroph in the context of methane conversion applications in biomanufacturing or methane emission mitigation in environments that experience dynamic fluxes of methane and oxygen.

MATERIALS AND METHODS

Strain. *M. album* BG8 was purchased from the American Type Culture Collection (catalog number 33003D). The genome of this strain has been sequenced (71) and is publicly available in the National Center for Biotechnology Information (NCBI) repository (assembly ASM21427v3), the Integrated Microbial Genomes (IMG) system (IMG genome ID 2508501010), and the KBase Central Store (source ID 686340.3).

Experimental procedures. For all of the experiments, *M. album* BG8 was cultured in 20 mL of nitrate mineral salts (NMS) medium (72) in a 160-mL serum bottle capped with a butyl rubber stopper. The initial bacterial cell concentration was adjusted according to the experimental specifications. For experiments with a relatively higher and lower initial biomass concentration (Fig. 7), the initial bacterial cell concentration was increased by 1.6-fold and decreased by 3.8-fold compared to all other experiments. The culture bottles were incubated at 30°C with agitation at 200 rpm, and $CuCl_2$ (5 μM) was used as the copper source (73). The headspace was filled with high-purity (99.995%) nitrogen, and the desired initial mixing ratio between oxygen and methane in the headspace was obtained by injecting appropriate volumes of the respective high-purity (99.7%) gases with a syringe. Here, the initial headspace volume-per-volume percentage refers to the reported percentages of oxygen and methane. All the experiments were performed with three biological replicates. Uninoculated controls were set up in parallel to assess abiotic losses (which were insignificant). For downstream analyses, the cells were collected on 0.22-μm filters (47 mm, MF-Millipore; MilliporeSigma, USA) and washed twice with sterile NMS medium.

Analytical analysis. To determine the headspace concentrations (mM) of hydrogen, oxygen, methane, and carbon dioxide, samples were collected using a gas-tight syringe (Hamilton, USA) and analyzed on a gas chromatograph (GC-2010; Shimadzu, Japan) as described previously (74). After withdrawing a gas sample, an equal volume of nitrogen gas was inserted into the headspace to make up the volume to avoid a vacuum effect (75). Excreted metabolites in the aqueous phase were measured using a high-performance liquid chromatography (HPLC) system (Waters Corporation, USA) equipped with an Aminex ion exclusion HPX-87H column (Bio-Rad, USA) as described previously (74).

Experimental measurement of biomass composition. The concentrations of cellular amino acids and total lipid fatty acids in bacterial cells were analyzed during the exponential growth phase. Seventeen amino acids were measured quantitatively using HPLC at the Proteomics and Metabolomics Facility, Center for Biotechnology, University of Nebraska-Lincoln (USA) by following standard protocols. The total levels of 15 lipid fatty acids were measured quantitatively using thin-layer chromatography, which was performed by a commercial laboratory (AminoAcids.com) by following standard protocols.

Conversion between the optical density and dry cell weight. To determine the conversion factor between the observed optical density at 600 nm (OD_{600}) and the dry cell weight (DCW), 13 cultures of *M. album* BG8 were grown under 20% methane and 20% oxygen to various cell densities (OD_{600} of 0.2 to 1.0), and the corresponding lyophilized cell masses were weighed. OD was measured using a UV-visible spectrophotometer (UV-1800, Shimadzu, Japan), and DCW was determined using an MS-TS analytical balance (MS204; Mettler, Toledo, OH).

Calculations of yield, rate, and flux. The yields of total biomass (gDCW mmol-CH_4^{-1}) and of specific metabolites (mmol mmol-CH_4^{-1}) were calculated by considering the changes in concentration per total methane consumed throughout the experiment. The growth rate (per hour) was calculated over the exponential phase as the log-linear regression between the biomass concentration and time. The specific uptake rate and excretion rate were considered equivalent to the uptake flux and excretion flux, respectively, when integrated as constraints into the GEM. To meet the steady-state assumption of the FBA, both rates or fluxes were calculated for each metabolite (in mmol h^{-1} $gDCW^{-1}$) in each experiment by linear regression of only those data points that were collected during the exponential phase, as described in a previously published protocol (76). Briefly, the growth rates were calculated using a linear regression between the log-biomass concentration and time, with the growth rate being the regression coefficient. The uptake/excretion of metabolites was calculated by using a linear regression between the metabolite concentration and the biomass concentration that was divided by the growth rate. The resulting regression coefficient was the flux, with a positive value indicating excretion and a negative value indicating uptake (76). The computed confidence intervals of the slopes in the linear regression model informed the uncertainty of the measured data and were applied as upper and lower constraints to the reactions in the GEM.

Reconstruction of a draft GEM. The GEM for *M. album* BG8 was reconstructed based on its genome sequence (71). A draft version of the model was reconstructed using KBase (43) and converted into Systems Biology Markup Language (SBML) for further curation and processing using the Sybil package in R (77), the COBRApy library in Python (78), and the COBRA Toolbox 3.0 in MATLAB (42).

***In silico* growth medium.** An *in silico* recipe of the chemical compounds required to produce biomass (i.e., growth medium) must be inputted into a GEM. All of the components in the experimental

NMS medium (72) were mapped to the KBase compounds database using the tools in the Known Media Database (KOMODO) (79). In the GEM, methane and nitrate were set as the sole carbon and nitrogen sources, respectively. The oxygen exchange reaction was set at a lower limit of -10 mmol h^{-1} $gDCW^{-1}$ to ensure an aerobic growth condition.

Integration of experimentally determined biomass compositions into the GEM. In a GEM, an accurate representation of the biomass composition enables better representations of the associated cellular biology and biochemistry. The biomass composition is specified using a metabolic reaction that accounts for the mass fraction of the different macromolecules that constitute 1 g of DCW. However, the automatically reconstructed GEM in KBase only generated a draft biomass production reaction in which the default biomass composition was generated according to the Gram classification of the bacterium of interest. To account for the experimentally determined biomass composition, the *M. album* BG8 biomass production reaction was manually edited using Python on the Jupyter Notebooks (80) interface of KBase. Briefly, the reaction was updated by adding the experimentally measured concentrations of amino acids and fatty acids and the intracellular organic metabolite, trace element, and cofactor concentrations used in the GEM of *M. buryatense* 5G(B1) (34). Pyrroloquinoline quinone (PQQ), a cofactor specific for methanol dehydrogenase, was added manually to the biomass production reaction. Other biomass components were obtained from the automatic KBase GEM reconstruction. The biomass production reaction in the GEM was then formulated using the stoichiometric coefficients of all of the metabolites required to generate 1 g of DCW. The following assumptions were made: growth-associated ATP maintenance of 59.8 mmol $gDCW^{-1}$, which is used in the GEMs of *Escherichia coli* (81) and other methanotrophs (34, 37), and non-growth-associated ATP maintenance of 3.5 mmol $gDCW^{-1}$ h^{-1}, as reported elsewhere for the methanotroph *M. parvus* OBBP (39). These ATP maintenance parameters have not been experimentally determined for *M. album* BG8; thus, they are a limitation of the current GEM.

Gap filling and model refinement. After the biomass production reaction in the GEM was edited as described in the previous section, automatic gap filling of the draft GEM was performed using KBase and components of the *in silico* NMS medium as the nutrient source. All of the reactions added in the gap-filling step were manually checked to determine their essentiality in the GEM using a leave-one-out approach, wherein single reactions were excluded and an FBA was applied to maximize the biomass production reaction. Reactions that were not essential to *in silico* biomass production were discarded.

After gap filling, the model was fine-tuned using an iterative refinement approach as described previously (42, 70). The gene-protein-reaction associations, reaction directionality, cofactor and coenzyme assignments, and Enzyme Commission numbers in the draft GEM were subjected to manual curation, using the following as references: (i) published literature, (ii) NCBI assembly annotations, (iii) BlastKOALA (82) genome annotation, (iv) RAST (83) genome annotation and the (v) KEGG (84), (vi) BRENDA (85), and (vii) KBase (43) reaction and metabolite databases.

The KBase-generated draft GEM in SBML format did not contain the chemical formulae of metabolites. The formulae from the KBase biochemistry database were manually integrated into the GEM. The balance of carbon, hydrogen, oxygen, and nitrogen was checked using the *checkBalance* function in the COBRA Toolbox 2.0. The final version of the *M. album* BG8 GEM was named *i*JV803 according to standard convention (86), where *i* stands for *in silico*, J and V are the initials of the name of the GEM builder, and 803 represents the number of included metabolic genes.

Gene locus tags in the GEM. *M. album* BG8 genes found in KBase (source ID 686340.3) were identified using locus tags that differed from those in the NCBI (accession no. NZ_CM001475) and Joint Genome Institute (genome ID 2508501010) depositories. To reconcile these differences and facilitate the use of the GEM in future research applications, all of the genes present in the GEM were aligned against genes identified in different repositories using Blast (87) (identity cutoff, 99%) to identify the corresponding locus tags. The annotations of all of the key genes involved in methane oxidation were further verified against the reported functions in the literature (24, 71), with no discrepancies. The locus tags of all of the genes in the GEM and their corresponding annotations in the different repositories are summarized in Table S1 in the supplemental material.

Quality control and quality assurance. The quality of the iJV803 GEM was checked using the MEMOTE platform (88), and a report of the model can be obtained at https://juanvillada.github.io/iJV803/docs/index.html.

Genome-scale metabolic modeling and FBA. FBA (44) was performed using the R package Sybil (77). To avoid infeasible metabolic cycles, the cycle-free FBA method (cfFBA) was also applied to metabolic modeling using the R package CycleFreeFlux (89). Linear programming problems were solved using the GNU Linear Programming kit (version 4.65). Although the objectives of optimization varied according to the objective of each analysis (90), the biomass production reaction was the default objective function in the GEM. The FBA method was applied in all phenotype phase plane analyses (91), whereas the cfFBA method was used to optimize parametrized GEMs. After normalizing the metabolic flux of each reaction to the methane specific uptake rate of each parametrized GEM, a principal-component analysis (PCA) of the metabolic fluxes of all reactions in the parametrized GEMs was performed using the R function *prcomp*.

Statistics. The *t* test was applied to test the difference between the mean of two groups, and analysis of variance (ANOVA) was applied to test the difference between more than two groups. The parametric tests were applied based on three criteria: (i) the Shapiro-Wilk test indicated a normal distribution, (ii) the variance of the samples was within the same order of magnitude, and (iii) the same number of independent samples was in each group. The majority approach was adopted when the criteria for parametric testing did not apply perfectly for some sample groups (as in the case for some of the data presented in Fig. 5F).

Data availability. The final version of the model can be downloaded in RData, SBML, JSON, and XLS formats from https://juanvillada.github.io/iJV803.

SUPPLEMENTAL MATERIAL

Supplemental material is available online only.

FIG S1, PDF file, 0.2 MB.

FIG S2, PDF file, 0.2 MB.

FIG S3, PDF file, 0.1 MB.

TABLE S1, XLS file, 1.5 MB.

TABLE S2, XLS file, 0.1 MB.

ACKNOWLEDGMENTS

This research was supported by the Research Grants Council of Hong Kong through project 11206514, the City University of Hong Kong through project 9678175, and the State Key Laboratory of Marine Pollution (SKLMP) Seed Collaborative Research Fund (SKLMP/IRF/0026). J.C.V. acknowledges support provided by the Hong Kong Ph.D. Fellowship Scheme (HKPFS).

J.C.V., M.F.D., C.K.L., and P.K.H.L. conceived the study. J.C.V. built the model and developed the scripts for data analysis. M.F.D. performed the experiments. J.C.V., M.F.D., and P.K.H.L. performed data analysis and interpreted the results. L.Y.S. contributed to the interpretation of the findings. J.C.V., M.F.D., L.Y.S., and P.K.H.L. wrote the manuscript. All authors approved the final version of the manuscript.

We declare that we have no competing interests.

REFERENCES

1. Nisbet EG, Manning MR, Dlugokencky EJ, Fisher RE, Lowry D, Michel SE, Myhre CL, Platt SM, Allen G, Bousquet P, Brownlow R, Cain M, France JL, Hermansen O, Hossaini R, Jones AE, Levin I, Manning AC, Myhre G, Pyle JA, Vaughn BH, Warwick NJ, White JWC. 2019. Very strong atmospheric methane growth in the 4 years 2014–2017: implications for the Paris agreement. Global Biogeochem Cycles 33:318–342. https://doi.org/10.1029/2018GB006009.
2. Solomon S, Daniel JS, Sanford TJ, Murphy DM, Plattner G-K, Knutti R, Friedlingstein P. 2010. Persistence of climate changes due to a range of greenhouse gases. Proc Natl Acad Sci U S A 107:18354–18359. https://doi.org/10.1073/pnas.1006282107.
3. Lee OK, Hur DH, Nguyen DTN, Lee EY. 2016. Metabolic engineering of methanotrophs and its application to production of chemicals and biofuels from methane. Biofuels Bioprod Bioref 10:848–863. https://doi.org/10.1002/bbb.1678.
4. Strong PJ, Xie S, Clarke WP. 2015. Methane as a resource: can the methanotrophs add value? Environ Sci Technol 49:4001–4018. https://doi.org/10.1021/es504242n.
5. AlSayed A, Fergala A, Eldyasti A. 2018. Sustainable biogas mitigation and value-added resources recovery using methanotrophs intergrated into wastewater treatment plants. Rev Environ Sci Biotechnol 17:351–393. https://doi.org/10.1007/s11157-018-9464-3.
6. Clomburg JM, Crumbley AM, Gonzalez R. 2017. Industrial biomanufacturing: the future of chemical production. Science 355:aag0804. https://doi.org/10.1126/science.aag0804.
7. Strong PJ, Kalyuzhnaya M, Silverman J, Clarke WP. 2016. A methanotroph-based biorefinery: potential scenarios for generating multiple products from a single fermentation. Bioresour Technol 215:314–323. https://doi.org/10.1016/j.biortech.2016.04.099.
8. Hwang IY, Nguyen AD, Nguyen TT, Nguyen LT, Lee OK, Lee EY. 2018. Biological conversion of methane to chemicals and fuels: technical challenges and issues. Appl Microbiol Biotechnol 102:3071–3080. https://doi.org/10.1007/s00253-018-8842-7.
9. Nguyen LT, Lee EY. 2019. Biological conversion of methane to putrescine using genome-scale model-guided metabolic engineering of a methanotrophic bacterium Methylomicrobium alcaliphilum 20Z. Biotechnol Biofuels 12:147. https://doi.org/10.1186/s13068-019-1490-z.
10. Henard CA, Akberdin IR, Kalyuzhnaya MG, Guarnieri MT. 2019. Muconic acid production from methane using rationally-engineered methanotrophic biocatalysts. Green Chem 21:6731–6737. https://doi.org/10.1039/C9GC03722E.
11. Milucka J, Kirf M, Lu L, Krupke A, Lam P, Littmann S, Kuypers MM, Schubert CJ. 2015. Methane oxidation coupled to oxygenic photosynthesis in anoxic waters. ISME J 9:1991–2002. https://doi.org/10.1038/ismej.2015.12.
12. Ettwig KF, Butler MK, Le Paslier D, Pelletier E, Mangenot S, Kuypers MM, Schreiber F, Dutilh BE, Zedelius J, de Beer D, Gloerich J, Wessels HJ, van Alen T, Luesken F, Wu ML, van de Pas-Schoonen KT, Op den Camp HJ, Janssen-Megens EM, Francoijs KJ, Stunnenberg H, Weissenbach J, Jetten MS, Strous M. 2010. Nitrite-driven anaerobic methane oxidation by oxygenic bacteria. Nature 464:543–548. https://doi.org/10.1038/nature08883.
13. Knittel K, Boetius A. 2009. Anaerobic oxidation of methane: progress with an unknown process. Annu Rev Microbiol 63:311–334. https://doi.org/10.1146/annurev.micro.61.080706.093130.
14. Boetius A, Ravenschlag K, Schubert CJ, Rickert D, Widdel F, Gieseke A, Amann R, Jørgensen BB, Witte U, Pfannkuche O. 2000. A marine microbial consortium apparently mediating anaerobic oxidation of methane. Nature 407:623–626. https://doi.org/10.1038/35036572.
15. Kalyuzhnaya MG. 2016. Chapter 13. Methane biocatalysis: selecting the right microbe, p 353–383. *In* Eckert CA, Trinh CT (ed), Biotechnology for biofuel production and optimization. Elsevier, Amsterdam, the Netherlands. https://doi.org/10.1016/B978-0-444-63475-7.00013-3.
16. Kalyuzhnaya MG, Kumaresan D, Heimann K, Caetano NS, Visvanathan C, Parthiba Karthikeyan O. 2020. Editorial–methane: a bioresource for fuel and biomolecules. Front Environ Sci https://doi.org/10.3389/fenvs.2020.00009.
17. Brantner CA, Remsen CC, Owen HA, Buchholz LA, Perille Collins ML. 2002. Intracellular localization of the particulate methane monooxygenase and methanol dehydrogenase in Methylomicrobium album BG8. Arch Microbiol 178:59–64. https://doi.org/10.1007/s00203-002-0426-2.
18. Kalyuzhnaya MG. 2016. Methylomicrobium, p 1–10. *In* Bergey's manual of systematics of archaea and bacteria. Springer-Verlag, New York, NY. https://doi.org/10.1002/9781118960608.gbm01182.pub2.
19. Orata FD, Meier-Kolthoff JP, Sauvageau D, Stein LY. 2018. Phylogenomic analysis of the Gammaproteobacterial methanotrophs (order Methylococcales) calls for the reclassification of members at the genus and species levels. Front Microbiol 9:3162. https://doi.org/10.3389/fmicb.2018.03162.

20. Bowman JP, Sly LI, Nichols PD, Hayward AC. 1993. Revised taxonomy of the methanotrophs: description of Methylobacter gen. nov., emendation of Methylococcus, validation of Methylosinus and Methylocystis species, and a proposal that the family Methylococcaceae includes only the group I methanotrophs. Int J Syst Evol Microbiol 43:735–753.
21. Miller LG, Baesman SM, Carlström CI, Coates JD, Oremland RS. 2014. Methane oxidation linked to chlorite dismutation. Front Microbiol 5:275. https://doi.org/10.3389/fmicb.2014.00275.
22. Vorobev A, Jagadevan S, Baral BS, Dispirito AA, Freemeier BC, Bergman BH, Bandow NL, Semrau JD. 2013. Detoxification of mercury by methanobactin from Methylosinus trichosporium OB3b. Appl Environ Microbiol 79:5918–5926. https://doi.org/10.1128/AEM.01673-13.
23. Campbell MA, Nyerges G, Kozlowski JA, Poret-Peterson AT, Stein LY, Klotz MG. 2011. Model of the molecular basis for hydroxylamine oxidation and nitrous oxide production in methanotrophic bacteria. FEMS Microbiol Lett 322:82–89. https://doi.org/10.1111/j.1574-6968.2011.02340.x.
24. Kits KD, Campbell DJ, Rosana AR, Stein LY. 2015. Diverse electron sources support denitrification under hypoxia in the obligate methanotroph Methylomicrobium album strain BG8. Front Microbiol 6:1072. https://doi.org/10.3389/fmicb.2015.01072.
25. Tays C, Guarnieri MT, Sauvageau D, Stein LY. 2018. Combined effects of carbon and nitrogen source to optimize growth of proteobacterial methanotrophs. Front Microbiol 9:2239. https://doi.org/10.3389/fmicb.2018.02239.
26. Nguyen AD, Lee EY. 2021. Engineered methanotrophy: a sustainable solution for methane-based industrial biomanufacturing. Trends Biotechnol 39:381–396. https://doi.org/10.1016/j.tibtech.2020.07.007.
27. Kalyuzhnaya MG, Puri AW, Lidstrom ME. 2015. Metabolic engineering in methanotrophic bacteria. Metab Eng 29:142–152. https://doi.org/10.1016/j.ymben.2015.03.010.
28. Nguyen DTN, Lee OK, Hadiyati S, Affifah AN, Kim MS, Lee EY. 2019. Metabolic engineering of the type I methanotroph Methylomonas sp. DH-1 for production of succinate from methane. Metab Eng 54:170–179. https://doi.org/10.1016/j.ymben.2019.03.013.
29. Nguyen DTN, Lee OK, Lim C, Lee J, Na JG, Lee EY. 2020. Metabolic engineering of type II methanotroph, Methylosinus trichosporium OB3b, for production of 3-hydroxypropionic acid from methane via a malonyl-CoA reductase-dependent pathway. Metab Eng 59:142–150. https://doi.org/10.1016/j.ymben.2020.02.002.
30. Nguyen AD, Hwang IY, Lee OK, Kim D, Kalyuzhnaya MG, Mariyana R, Hadiyati S, Kim MS, Lee EY. 2018. Systematic metabolic engineering of Methylomicrobium alcaliphilum 20Z for 2,3-butanediol production from methane. Metab Eng 47:323–333. https://doi.org/10.1016/j.ymben.2018.04.010.
31. Nguyen AD, Kim D, Lee EY. 2020. Unlocking the biosynthesis of sesquiterpenoids from methane via the methylerythritol phosphate pathway in methanotrophic bacteria, using α-humulene as a model compound. Metab Eng 61:69–78. https://doi.org/10.1016/j.ymben.2020.04.011.
32. Nguyen TT, Lee OK, Naizabekov S, Lee EY. 2020. Bioconversion of methane to cadaverine and lysine using an engineered type II methanotroph, Methylosinus trichosporium OB3b. Green Chem 22:7803–7811. https://doi.org/10.1039/D0GC02232B.
33. Duc Nguyen A, Hoang Trung Chau T, Yeol Lee E. 2021. Methanotrophic microbial cell factory platform for simultaneous conversion of methane and xylose to value-added chemicals. Chem Eng J 420:127632. https://doi.org/10.1016/j.cej.2020.127632.
34. de la Torre A, Metivier A, Chu F, Laurens LML, Beck DAC, Pienkos PT, Lidstrom ME, Kalyuzhnaya MG. 2015. Genome-scale metabolic reconstructions and theoretical investigation of methane conversion in Methylomicrobium buryatense strain 5G(B1). Microb Cell Fact 14:188. https://doi.org/10.1186/s12934-015-0377-3.
35. Akberdin IR, Thompson M, Hamilton R, Desai N, Alexander D, Henard CA, Guarnieri MT, Kalyuzhnaya MG. 2018. Methane utilization in Methylomicrobium alcaliphilum 20Z(R): a systems approach. Sci Rep 8:2512. https://doi.org/10.1038/s41598-018-20574-z.
36. Lieven C, Petersen LAH, Jørgensen SB, Gernaey KV, Herrgard MJ, Sonnenschein N. 2018. A genome-scale metabolic model for Methylococcus capsulatus (Bath) suggests reduced efficiency electron transfer to the particulate methane monooxygenase. Front Microbiol 9:2947. https://doi.org/10.3389/fmicb.2018.02947.
37. Gupta A, Ahmad A, Chothwe D, Madhu MK, Srivastava S, Sharma VK. 2019. Genome-scale metabolic reconstruction and metabolic versatility of an obligate methanotroph Methylococcus capsulatus str Bath. PeerJ 7:e6685. https://doi.org/10.7717/peerj.6685.
38. Bordel S, Rodriguez Y, Hakobyan A, Rodriguez E, Lebrero R, Munoz R. 2019. Genome scale metabolic modeling reveals the metabolic potential of three type II methanotrophs of the genus Methylocystis. Metab Eng 54:191–199. https://doi.org/10.1016/j.ymben.2019.04.001.
39. Bordel S, Rojas A, Muñoz R. 2019. Reconstruction of a genome scale metabolic model of the polyhydroxybutyrate producing methanotroph Methylocystis parvus OBBP. Microb Cell Fact 18:104. https://doi.org/10.1186/s12934-019-1154-5.
40. Bordel S, Crombie AT, Muñoz R, Murrell JC. 2020. Genome scale metabolic model of the versatile methanotroph Methylocella silvestris. Microb Cell Fact 19:144. https://doi.org/10.1186/s12934-020-01395-0.
41. Naizabekov S, Lee EY. 2020. Genome-scale metabolic model reconstruction and in silico investigations of methane metabolism in Methylosinus trichosporium OB3b. Microorganisms 8:437. https://doi.org/10.3390/microorganisms8030437.
42. Heirendt L, Arreckx S, Pfau T, Mendoza SN, Richelle A, Heinken A, Haraldsdottir HS, Wachowiak J, Keating SM, Vlasov V, Magnusdottir S, Ng CY, Preciat G, Zagare A, Chan SHJ, Aurich MK, Clancy CM, Modamio J, Sauls JT, Noronha A, Bordbar A, Cousins B, El Assal DC, Valcarcel LV, Apaolaza I, Ghaderi S, Ahookhosh M, Ben Guebila M, Kostromins A, Sompairac N, Le HM, Ma D, Sun Y, Wang L, Yurkovich JT, Oliveira MAP, Vuong PT, El Assal LP, Kuperstein I, Zinovyev A, Hinton HS, Bryant WA, Aragon Artacho FJ, Planes FJ, Stalidzans E, Maass A, Vempala S, Hucka M, Saunders MA, Maranas CD, et al. 2019. Creation and analysis of biochemical constraint-based models using the COBRA toolbox v.3.0. Nat Protoc 14:639–702. https://doi.org/10.1038/s41596-018-0098-2.
43. Arkin AP, Cottingham RW, Henry CS, Harris NL, Stevens RL, Maslov S, Dehal P, Ware D, Perez F, Canon S, Sneddon MW, Henderson ML, Riehl WJ, Murphy-Olson D, Chan SY, Kamimura RT, Kumari S, Drake MM, Brettin TS, Glass EM, Chivian D, Gunter D, Weston DJ, Allen BH, Baumohl J, Best AA, Bowen B, Brenner SE, Bun CC, Chandonia J-M, Chia J-M, Colasanti R, Conrad N, Davis JJ, Davison BH, DeJongh M, Devoid S, Dietrich E, Dubchak I, Edirisinghe JN, Fang G, Faria JP, Frybarger PM, Gerlach W, Gerstein M, Greiner A, Gurtowski J, Haun HL, He F, Jain R, et al. 2018. KBase: the United States Department of Energy Systems Biology knowledgebase. Nat Biotechnol 36:566–569. https://doi.org/10.1038/nbt.4163.
44. Orth JD, Thiele I, Palsson BØ. 2010. What is flux balance analysis? Nat Biotechnol 28:245–248. https://doi.org/10.1038/nbt.1614.
45. Segrè D, Vitkup D, Church GM. 2002. Analysis of optimality in natural and perturbed metabolic networks. Proc Natl Acad Sci U S A 99:15112–15117. https://doi.org/10.1073/pnas.232349399.
46. Markou G, Vandamme D, Muylaert K. 2014. Ammonia inhibition on Arthrospira platensis in relation to the initial biomass density and pH. Bioresour Technol 166:259–265. https://doi.org/10.1016/j.biortech.2014.05.040.
47. Wijffels RH, Schepers AW, Smit M, de Gooijer CD, Tramper J. 1994. Effect of initial biomass concentration on the growth of immobilized Nitrosomonas europaea. Appl Microbiol Biotechnol 42:153–157. https://doi.org/10.1007/BF00170239.
48. Chen Z, Huang L, Wen Q, Zhang H, Guo Z. 2017. Effects of sludge retention time, carbon and initial biomass concentrations on selection process: from activated sludge to polyhydroxyalkanoate accumulating cultures. J Environ Sci (China) 52:76–84. https://doi.org/10.1016/j.jes.2016.03.014.
49. Wang J, Han D, Sommerfeld MR, Lu C, Hu Q. 2013. Effect of initial biomass density on growth and astaxanthin production of Haematococcus pluvialis in an outdoor photobioreactor. J Appl Phycol 25:253–260. https://doi.org/10.1007/s10811-012-9859-4.
50. Eker S, Sarp M. 2017. Hydrogen gas production from waste paper by dark fermentation: effects of initial substrate and biomass concentrations. Int J Hydrogen Energy 42:2562–2568. https://doi.org/10.1016/j.ijhydene.2016.04.020.
51. Graham DW, Chaudhary JA, Hanson RS, Arnold RG. 1993. Factors affecting competition between type I and type II methanotrophs in two-organism, continuous-flow reactors. Microb Ecol 25:17. https://doi.org/10.1007/BF00182126.
52. Han JI, Semrau JD. 2000. Chloromethane stimulates growth of Methylomicrobium album BG8 on methanol. FEMS Microbiol Lett 187:77–81. https://doi.org/10.1111/j.1574-6968.2000.tb09140.x.
53. Benstead J, King GM, Williams HG. 1998. Methanol promotes atmospheric methane oxidation by methanotrophic cultures and soils. Appl Environ Microbiol 64:1091–1098. https://doi.org/10.1128/AEM.64.3.1091-1098.1998.
54. Stone K, Hilliard M, Badr K, Bradford A, He QP, Wang J. 2020. Comparative study of oxygen-limited and methane-limited growth phenotypes of Methylomicrobium buryatense 5GB1. Biochem Eng J 161:107707. https://doi.org/10.1016/j.bej.2020.107707.
55. Sugden S, Lazic M, Sauvageau D, Stein LY. 2021. Transcriptomic and metabolomic responses to carbon and nitrogen sources in Methylomicrobium

album BG8. Appl Environ Microbiol 87:e00385-21. https://doi.org/10.1128/AEM.00385-21.
56. Bang J, Hwang CH, Ahn JH, Lee JA, Lee SY. 2020. Escherichia coli is engineered to grow on CO2 and formic acid. Nat Microbiol 5:1459–1463. https://doi.org/10.1038/s41564-020-00793-9.
57. Bang J, Lee SY. 2018. Assimilation of formic acid and CO2 by engineered Escherichia coli equipped with reconstructed one-carbon assimilation pathways. Proc Natl Acad Sci U S A 115:E9271–E9279. https://doi.org/10.1073/pnas.1810386115.
58. Lu H, Villada JC, Lee PKH. 2019. Modular metabolic engineering for biobased chemical production. Trends Biotechnol 37:152–166. https://doi.org/10.1016/j.tibtech.2018.07.003.
59. Gilman A, Laurens LM, Puri AW, Chu F, Pienkos PT, Lidstrom ME. 2015. Bioreactor performance parameters for an industrially-promising methanotroph Methylomicrobium buryatense 5GB1. Microb Cell Fact 14:182. https://doi.org/10.1186/s12934-015-0372-8.
60. Fu Y, He L, Reeve J, Beck DAC, Lidstrom ME. 2019. Core metabolism shifts during growth on methanol versus methane in the methanotroph Methylomicrobium buryatense 5GB1. mBio 10:e00406-19. https://doi.org/10.1128/mBio.00406-19.
61. Nguyen AD, Park JY, Hwang IY, Hamilton R, Kalyuzhnaya MG, Kim D, Lee EY. 2020. Genome-scale evaluation of core one-carbon metabolism in gammaproteobacterial methanotrophs grown on methane and methanol. Metab Eng 57:1–12. https://doi.org/10.1016/j.ymben.2019.10.004.
62. Kiefer D, Merkel M, Lilge L, Henkel M, Hausmann R. 2021. From acetate to bio-based products: underexploited potential for industrial biotechnology. Trends Biotechnol 39:397–411. https://doi.org/10.1016/j.tibtech.2020.09.004.
63. Gilman A, Fu Y, Hendershott M, Chu F, Puri AW, Smith AL, Pesesky M, Lieberman R, Beck DAC, Lidstrom ME. 2017. Oxygen-limited metabolism in the methanotroph Methylomicrobium buryatense 5GB1C. PeerJ 5:e3945. https://doi.org/10.7717/peerj.3945.
64. Kalyuzhnaya MG, Yang S, Rozova ON, Smalley NE, Clubb J, Lamb A, Gowda GA, Raftery D, Fu Y, Bringel F, Vuilleumier S, Beck DA, Trotsenko YA, Khmelenina VN, Lidstrom ME. 2013. Highly efficient methane biocatalysis revealed in a methanotrophic bacterium. Nat Commun 4:2785. https://doi.org/10.1038/ncomms3785.
65. Hakobyan A, Zhu J, Glatter T, Paczia N, Liesack W. 2020. Hydrogen utilization by Methylocystis sp. strain SC2 expands the known metabolic versatility of type IIa methanotrophs. Metab Eng 61:181–196. https://doi.org/10.1016/j.ymben.2020.05.003.
66. Amaral JA, Knowles R. 1995. Growth of methanotrophs in methane and oxygen counter gradients. FEMS Microbiol Lett 126:215–220. https://doi.org/10.1111/j.1574-6968.1995.tb07421.x.
67. Joergensen L, Degn H. 1983. Mass spectrometric measurements of methane and oxygen utilization by methanotrophic bacteria. FEMS Microbiol Lett 20:331–335. https://doi.org/10.1111/j.1574-6968.1983.tb00142.x.
68. Chidambarampadmavathy K, Karthikeyan OP, Huerlimann R, Maes GE, Heimann K. 2017. Response of mixed methanotrophic consortia to different methane to oxygen ratios. Waste Manag 61:220–228. https://doi.org/10.1016/j.wasman.2016.11.007.
69. Varma A, Palsson BO. 1994. Stoichiometric flux balance models quantitatively predict growth and metabolic by-product secretion in wild-type Escherichia coli W3110. Appl Environ Microbiol 60:3724–3731. https://doi.org/10.1128/aem.60.10.3724-3731.1994.
70. Thiele I, Palsson BØ. 2010. A protocol for generating a high-quality genome-scale metabolic reconstruction. Nat Protoc 5:93–121. https://doi.org/10.1038/nprot.2009.203.
71. Kits KD, Kalyuzhnaya MG, Klotz MG, Jetten MS, Op den Camp HJ, Vuilleumier S, Bringel F, Dispirito AA, Murrell JC, Bruce D, Cheng JF, Copeland A, Goodwin L, Hauser L, Lajus A, Land ML, Lapidus A, Lucas S, Medigue C, Pitluck S, Woyke T, Zeytun A, Stein LY. 2013. Genome sequence of the obligate Gammaproteobacterial methanotroph Methylomicrobium album strain BG8. Genome Announc 1:e00170-13. https://doi.org/10.1128/genomeA.00170-13.
72. Whittenbury R, Phillips KC, Wilkinson JF. 1970. Enrichment, isolation and some properties of methane-utilizing bacteria. Microbiology 61:205–218.
73. Collins ML, Buchholz LA, Remsen CC. 1991. Effect of copper on Methylomonas albus BG8. Appl Environ Microbiol 57:1261–1264. https://doi.org/10.1128/aem.57.4.1261-1264.1991.
74. Lu H, Lee PKH. 2015. Effects of cellulose concentrations on the syntrophic interactions between Clostridium cellulovorans 743B and Rhodopseudomonas palustris CGA009 in coculture fermentation for biohydrogen production. Int J Hydrogen Energy 40:11800–11808. https://doi.org/10.1016/j.ijhydene.2015.05.135.
75. Stone KA, He QP, Wang J. 2019. Two experimental protocols for accurate measurement of gas component uptake and production rates in bioconversion processes. Sci Rep 9:5899. https://doi.org/10.1038/s41598-019-42469-3.
76. Dias O, Rocha M, Ferreira EC, Rocha I. 2018. Reconstructing high-quality large-scale metabolic models with Merlin. Methods Mol Biol 1716:1–36. https://doi.org/10.1007/978-1-4939-7528-0_1.
77. Gelius-Dietrich G, Desouki AA, Fritzemeier CJ, Lercher MJ. 2013. Sybil–efficient constraint-based modelling in R. BMC Syst Biol 7:125. https://doi.org/10.1186/1752-0509-7-125.
78. Ebrahim A, Lerman JA, Palsson BO, Hyduke DR. 2013. COBRApy: constraints-based reconstruction and analysis for Python. BMC Syst Biol 7:74. https://doi.org/10.1186/1752-0509-7-74.
79. Oberhardt MA, Zarecki R, Gronow S, Lang E, Klenk H-P, Gophna U, Ruppin E. 2015. Harnessing the landscape of microbial culture media to predict new organism–media pairings. Nat Commun 6:8493. https://doi.org/10.1038/ncomms9493.
80. Kluyver T, Ragan-Kelley B, Perez F, Granger B, Bussonnier M, Frederic J, Kelley K, Hamrick J, Grout J, Corlay S, Ivanov P, Avila D, Abdalla S, Willing C, Jupyter Development Team. 2016. Jupyter notebooks–a publishing format for reproducible computational workflows. 20th Int Conf Electronic Pub, p 87–90.
81. Feist AM, Henry CS, Reed JL, Krummenacker M, Joyce AR, Karp PD, Broadbelt LJ, Hatzimanikatis V, Palsson BØ. 2007. A genome-scale metabolic reconstruction for Escherichia coli K-12 MG1655 that accounts for 1260 ORFs and thermodynamic information. Mol Syst Biol 3:121. https://doi.org/10.1038/msb4100155.
82. Kanehisa M, Sato Y, Morishima K. 2016. BlastKOALA and GhostKOALA: KEGG tools for functional characterization of genome and metagenome sequences. J Mol Biol 428:726–731. https://doi.org/10.1016/j.jmb.2015.11.006.
83. Overbeek R, Olson R, Pusch GD, Olsen GJ, Davis JJ, Disz T, Edwards RA, Gerdes S, Parrello B, Shukla M, Vonstein V, Wattam AR, Xia F, Stevens R. 2014. The SEED and the rapid annotation of microbial genomes using subsystems technology (RAST). Nucleic Acids Res 42:D206–D214. https://doi.org/10.1093/nar/gkt1226.
84. Kanehisa M, Goto S. 2000. KEGG: Kyoto encyclopedia of genes and genomes. Nucleic Acids Res 28:27–30. https://doi.org/10.1093/nar/28.1.27.
85. Schomburg I, Jeske L, Ulbrich M, Placzek S, Chang A, Schomburg D. 2017. The BRENDA enzyme information system–from a database to an expert system. J Biotechnol 261:194–206. https://doi.org/10.1016/j.jbiotec.2017.04.020.
86. Jensen CS, Norsigian CJ, Fang X, Nielsen XC, Christensen JJ, Palsson BO, Monk JM. 2020. Reconstruction and validation of a genome-scale metabolic model of Streptococcus oralis (iCJ415), a human commensal and opportunistic pathogen. Front Genet 11:116. https://doi.org/10.3389/fgene.2020.00116.
87. Altschul SF, Gish W, Miller W, Myers EW, Lipman DJ. 1990. Basic local alignment search tool. J Mol Biol 215:403–410. https://doi.org/10.1016/S0022-2836(05)80360-2.
88. Lieven C, Beber ME, Olivier BG, Bergmann FT, Ataman M, Babaei P, Bartell JA, Blank LM, Chauhan S, Correia K, Diener C, Dräger A, Ebert BE, Edirisinghe JN, Faria JP, Feist AM, Fengos G, Fleming RMT, García-Jiménez B, Hatzimanikatis V, van Helvoirt W, Henry CS, Hermjakob H, Herrgård MJ, Kaafarani A, Kim HU, King Z, Klamt S, Klipp E, Koehorst JJ, König M, Lakshmanan M, Lee D-Y, Lee SY, Lee S, Lewis NE, Liu F, Ma H, Machado D, Mahadevan R, Maia P, Mardinoglu A, Medlock GL, Monk JM, Nielsen J, Nielsen LK, Nogales J, Nookaew I, Palsson BO, Papin JA, et al. 2020. MEMOTE for standardized genome-scale metabolic model testing. Nat Biotechnol 38:272–276. https://doi.org/10.1038/s41587-020-0446-y.
89. Desouki AA, Jarre F, Gelius-Dietrich G, Lercher MJ. 2015. CycleFreeFlux: efficient removal of thermodynamically infeasible loops from flux distributions. Bioinformatics 31:2159–2165. https://doi.org/10.1093/bioinformatics/btv096.
90. Feist AM, Palsson BO. 2010. The biomass objective function. Curr Opin Microbiol 13:344–349. https://doi.org/10.1016/j.mib.2010.03.003.
91. Edwards JS, Ramakrishna R, Palsson BO. 2002. Characterizing the metabolic phenotype: a phenotype phase plane analysis. Biotechnol Bioeng 77:27–36. https://doi.org/10.1002/bit.10047.